Title
- Full title: Coupling chromatin structure and dynamics by live super-resolution imaging
- Short title: Coupling chromatin structure and dynamics

Authors

R. Barth[1, 2,] K. Bystricky[1] and H. A. Shaban[,1, 3, †, *]

Affiliations

1: Laboratoire de Biologie Moléculaire Eucaryote (LBME), Centre de Biologie Intégrative (CBI), CNRS; University of Toulouse, UPS; 31062 Toulouse; France. 2: Department of Bionanoscience, Delft University of Technology, 2628 CJ Delft, The Netherlands. 3: Spectroscopy Department, Physics Division, National Research Centre, Dokki, 12622 Cairo, Egypt.

†: Present address: Center for Advanced Imaging, Northwest Building, Harvard University, Cambridge, MA, 02138, USA.

*: To whom correspondence may be addressed: Haitham A. Shaban. Email hshaban@fas.harvard.edu

Abstract

Chromatin conformation regulates gene expression and thus constant remodeling of chromatin structure is essential to guarantee proper cell function. To gain insight into the spatio-temporal organization of the genome, we employ high-density photo-activated localization microscopy and deep learning to obtain temporally resolved super-resolution images of chromatin *in vivo*. In combination with high-resolution dense motion reconstruction, we confirm the existence of elongated ~ 45 to 90 nm wide chromatin 'blobs', which appear to be dynamically associating chromatin fragments in close physical and genomic proximity and adopt TAD-like interactions in the time-average limit. We found the chromatin structure exhibits a spatio-temporal correlation extending ~ 4 μm in space and tens of seconds in time, while chromatin dynamics are correlated over ~ 6 μm and outlast 40 s. Notably, chromatin structure and dynamics are closely interrelated, which may constitute a mechanism to grant access to regions with high local chromatin concentration.

Introduction

The three-dimensional organization of the eukaryotic genome plays a central role in gene regulation (1–3). Its spatial organization has been prominently characterized by molecular and cellular approaches including high-throughput chromosome conformation capture (Hi-C) (4) and fluorescent in situ hybridization (FISH) (5). Topologically associated domains (TADs), genomic regions that display a high degree of interaction, were revealed and found to be a key architectural feature (6). Direct 3D localization microscopy of the chromatin fiber at the nanoscale (7) confirmed the presence of TADs in single cells but also, among others, revealed great structural variation of chromatin architecture (8, 9). To comprehensively resolve the spatial heterogeneity of chromatin, super-resolution microscopy must be employed. Previous work showed that nucleosomes are distributed as segregated, nanometer-sized accumulations throughout the nucleus (10–13) and that the epigenetic state of a locus has a large impact on its folding (14, 15). However, to resolve the fine structure of chromatin, high labeling densities, long acquisition times and, often, cell fixation are required. This precludes capturing dynamic processes of chromatin in single live cells, yet chromatin moves at different spatial and temporal scales.

The first efforts to relate chromatin organization and its dynamics were made using a combination of Photo-activated Localization Microscopy (PALM) and tracking of single nucleosomes (16). It could be shown that nucleosomes mostly move coherently with their underlying domains, in accordance with conventional microscopy data (17); however, a quantitative link between the observed dynamics and the surrounding chromatin structure could not yet be established in real-time. Although it is becoming increasingly clear that chromatin motion and long-range interactions are key to genome organization and gene regulation (18), tools to detect and to define bulk chromatin motion simultaneously at divergent spatio-temporal scales and high resolution are still missing.

56   Here we apply deep learning-based photo-activated localization microscopy (Deep-PALM) for

57   temporally resolved super-resolution imaging of chromatin *in vivo*. Deep-PALM acquires a single

58   resolved image in a few hundred milliseconds with a spatial resolution of ~ 60 nm. We observed

59   elongated ~ 45 to 90 nm wide chromatin domain 'blobs'. Employing a computational chromosome

60   model, we inferred that blobs are highly dynamic entities, which dynamically assemble and

61   disassemble. Consisting of chromatin in close physical and genomic proximity, blobs nevertheless

62   adopt TAD-like interaction patterns when chromatin confirmations are averaged over time. Using

63   a combination of Deep-PALM and high-resolution dense motion reconstruction (*17*), we

64   simultaneously analyzed both structural and dynamic properties of chromatin. Our analysis

65   emphasizes the presence of spatio-temporal cross-correlations between chromatin structure and

66   dynamics, extending several micrometers in space and tens of seconds in time. Furthermore,

67   extraction and statistical mapping of multiple observables from the dynamic behavior of chromatin

68   blobs shows that local chromatin density regulates local chromatin dynamics.

69

70   **Results**

71   **Deep-PALM reveals dynamical chromatin remodeling in living cells.**

72   Super-resolution imaging of complex and compact macromolecules such as chromatin requires

73   dense labeling of the chromatin fiber in order to resolve fine features. We employ Deep-STORM,

74   a method which uses a deep convolutional neural network (CNN) to predict super-resolution images

75   from stochastically blinking emitters (*19*) (Figure 1A; Materials and Methods). The CNN was

76   trained to specific labeling densities for live-cell chromatin imaging using a photo-activated

77   fluorophore (PATagRFP); we therefore refer to the method as Deep-PALM. We chose three

78   labeling densities 4, 6 and 9 emitters per μm^2 per frame in the ON-state to test, based on the

79   comparison of simulated and experimental wide field images (Supplementary Figure 1A). The

80   CNN trained with 9 emitters per μm^2 performed significantly worse than the other CNNs and was

81 thus excluded from further analysis (Supplementary Figure 1B; Materials and Methods). We

82 applied Deep-PALM to reconstruct an image set of labeled histone protein (H2B-PATagRFP) in

83 human bone osteosarcoma (U2OS) cells using the networks trained on 4 and 6 emitters per μm^2 per

84 frame (Materials and Methods). A varying number of predictions by the CNN of each individual

85 frame of the input series were summed to reconstruct a temporal series of super resolved images

86 (Supplementary Figure 1C). The predictions made by the CNN trained with 4 emitters per μm^2

87 show large spaces devoid of signal intensity, especially at the nuclear periphery, making this CNN

88 inadequate for live-cell super-resolution imaging of chromatin. While collecting photons from long

89 acquisitions for super-resolution imaging is desirable in fixed cells, Deep-PALM is a live imaging

90 approach. Summing over many individual predictions leads to considerable motion blur and thus

91 loss in resolution. Quantitatively, the Nyquist criterion states that the image resolution $R = 2/\sqrt{\tau\rho}$

92 depends on ρ, the localization density per second and the time resolution τ (20). In contrast, motion

93 blur strictly depends on the diffusion constant D of the underlying structure $R = \sqrt{4D\tau}$. There is

94 thus an optimum resolution due to the tradeoff between increased emitter sampling and the

95 avoidance of motion blur, which was at a time resolution of 360 ms for our experiments (Figure

96 1B; Supplementary Figure 1D). Super-resolution imaging of H2B-PATagRFP in live cells at this

97 temporal resolution shows a pronounced nuclear periphery while fluorescent signals in the interior

98 vary in intensity (Figure 1C). This likely corresponds to chromatin-rich and chromatin-poor regions

99 (13). These regions rearrange over time, reflecting the dynamic behavior of bulk chromatin.

100 Chromatin-rich and chromatin-poor regions were visible not only at the scale of the whole-nucleus,

101 but also at the resolution of a few hundred nanometers (Figure 1D). Within chromatin-rich regions,

102 the intensity distribution was not uniform but exhibited spatially segregated accumulations of

103 labeled histones of variable shape and size, reminiscent of nucleosome clutches (10), nanodomains

104 (14, 16) or TADs (21). At the nuclear periphery, prominent structures arise. Certain chromatin

105 structures could be observed for ~ 1 s, which underwent conformational changes during this period

106   (Figure 1E). The spatial resolution at which structural elements can be observed (Materials and

107   Methods) in time-resolved super-resolution data of chromatin was 63 ± 2 nm (Figure 1E), slightly

108   more optimistic than the theoretical prediction (Figure 1B) (*22*). Thus, Deep-PALM identifies

109   spatially heterogeneous coverage of chromatin as previously reported (*10*, *13*, *14*, *16*, *21*). We

110   further monitor chromatin temporally at nanometer scale in living cells.

111

Chromatin appears in elongated nanometer-sized blobs with a non-random spatial

distribution.

114   To quantitatively assess the spatial distribution of H2B, we developed an image segmentation

115   scheme (Materials and Methods, Supplementary Figure 2) which allowed us to segment spatially

116   separated accumulations of H2B signal with high fidelity (Supplementary Note 1, Supplementary

117   Figure 3, Supplementary Figure 4). Applying our segmentation scheme, $\sim 10{,}000$ separable

118   elements, blob-like structures were observed for each super-resolved image (166 resolved images

119   per movie; Figure 2A). To elucidate their origin and formation, we used a transferable

120   computational model introduced by Qi *et al.* (*23*), which is based on one-dimensional genomics

121   and epigenomics data, including histone modification profiles and CTCF binding sites. Super-

122   resolution images were generated from the modeled chromosomes. Within these images we

123   identified and characterized 'chromatin blobs' analogously as for experimental data (Materials and

124   Methods; Figure 2B).

125   For both imaged and modeled chromatin, we first computed the kth nearest neighbor distance (NND;

126   centroid-to-centroid) distributions, taking into account the nearest 1st to 40th neighbors (Figure 2C,

127   blue to red). Centroids of nearest neighbors are (95 ± 30) nm (mean $\pm$ standard deviation) apart,

128   consistent with previous super-resolution images of chromatin in fixed cells (*14*) and slightly

129   further than what was found for clutches of nucleosomes (*10*). The envelope of all NND

130   distributions (Figure 2C, black line) shows several weak maxima at ~ 95 nm, 235 nm, 335 nm, and

131   450 nm, which roughly coincide with the peaks of the 1st, 7th, 14th and 25th nearest neighbors

132   respectively (Figure 2C, red dots). In contrast, simulated data exhibit a prominent first nearest

133   neighbor peak at slightly smaller distance and higher-order NND distribution decay quickly and

134   appear washed out (Figure 2D). This hints towards greater levels of spatial organization of

135   chromatin *in vivo*, which is not readily recapitulated in the employed state-of-the-art chromosome

136   model.

137   Next, we were interested in the typical size of chromatin blobs. Their area distribution (Figure 2E)

138   fit a log-normal distribution with parameters $(3.3 \pm 2.8) \cdot 10^{-3}$ μm^2 (mean $\pm$ standard deviation),

139   which is in line with the area distribution derived from modeled chromosomes. Notably, blob areas

140   vary considerably as indicated by the high standard deviation and the prominent tail of the area

141   distribution towards large values. Following this we calculated the eccentricity of each blob to

142   resolve their shape (Figure 2F). The eccentricity is a measure of the elongation of a region reflecting

143   the ratio of the longest chord of the shape and the shortest chord perpendicular to it (Figure 2F,

144   illustrated shapes at selected eccentricity values). The distribution of eccentricity values shows an

145   accumulation of values close to 1, with a peak value of ~ 0.9, which shows that most blobs have an

146   elongated, fiber-like shape and are not circular. In particular, the eccentricity value of 0.9

147   corresponds to a ratio between the short and long axis of the ellipse of ~ ½ (Materials and Methods),

148   which results, considering the typical area of blobs, in roughly 92 nm long and 46 nm wide blobs

149   on average. The length coincides with the value found for the typical nearest-neighbor distance

150   (Figure 2C; (95 ± 30) nm). However, due to the segregation of chromatin into blobs, their

151   elongated shape and their random orientation (Figure 2A), the blobs cannot be closely packed

152   throughout the nucleus. We find that chromatin has a spatially heterogeneous density, occupying 5

153   - 60% of the nuclear area (Supplementary Figure 5A, B), which is supported by a previous electron

154   microscopy study (*24*). The blob dimensions also fall within previously determined size ranges (*10*,

155   *14*), confirming the existence of spatially segregated chromatin structures in the sub-100 nm range.

Chromatin blobs identified by Deep-PALM are coherent with sub-TADs

Due to the projection of the nuclear volume to the imaging plane, the observed blobs could simply be overlays of distant, along the one-dimensional genome, non-interacting genomic loci. To exclude this possibility, we analyzed the gap length along the simulated chromosome between beads belonging to the same blob. The analysis showed that the blobs are mostly made of consecutive beads along the genome, thus implying an underlying domain-like structure, similar to TADs (Figure 3A). Using the affiliation of each bead to an intrinsic chromatin state of the model (Figure 3B), it became apparent that blobs along the simulated chromosome consisting mostly of active chromatin are significantly larger than those formed by inactive and repressive chromatin (Figure 3C). These findings are in line with experimental results (*15*) and results from the simulations directly (*23*), thereby validating the projection and segmentation process.

Since chromatin is dynamic *in vivo* and in computer simulations, each bead can diffuse in and out of the imaging volume from frame to frame. We estimated that, on average, each bead spent approximately 1.5 s continuously within a slab of 200 nm thickness (Figure 3D). Furthermore, a bead is on average found only 0.55 ± 0.33 s continuously within a blob, which corresponds to $1 - 2$ experimental super-resolved images (Figure 3D). These results suggest that chromatin blobs are highly dynamic entities, which usually form and dissemble within less than one second. We thus constructed a time-averaged association map for the modeled chromosomes, quantifying the frequency at which each locus is found with any other locus within one blob. The association map is comparable to interaction maps derived from Hi-C (Figure 3E). Strikingly, inter-loci association and Hi-C maps are strongly correlated, and the association map shows similar patterns as those identified as TADs in Hi-C maps, even for relatively distant genomic loci (> 1 Mbp). A similar TAD-like organization is also apparent when the average inverse distance between loci is considered (Figure 3F, upper panel), suggesting that blobs could be identified in super-resolved images due to the proximity of loci within blobs in physical space. Using the computational

181   chromosome model, we conclude that chromatin blobs identified by Deep-PALM are mostly made

182   of continuous regions along the genome and cannot be attributed to artifacts originating from the

183   projection of the three-dimensional genome structure to the imaging plane. The blobs associate and

184   dissociate within less than one second, but loci within blobs are likely to belong to the same TAD.

185   Their average genomic content is 75 kb, only a fraction of typical TAD lengths in mammalian cells

186   (average size 880 kb) (*6*), suggesting that blobs likely correspond to sub-TADs or TAD nano-

187   compartments (*21*).

188

189   **Super-resolution chromatin dynamics using Deep-PALM**

190   To quantify the experimentally observed chromatin dynamics at the nanoscale, down to the size of

191   one pixel (13.5 nm), we used a dense reconstruction of flow fields, Optical Flow (OF; Figure 4A,

192   Materials and Methods), which was previously used to analyze images taken on confocal (*25*, *26*),

193   and Structured Illumination Microscopes (*13*). We examined the suitability of OF for super-

194   resolution based on single molecule localization images using simulations. We find that the

195   accuracy of OF is slightly enhanced on super-resolved images, compared to conventional

196   fluorescence microscopy images (Supplementary Note 2, Supplementary Figure 6). Experimental

197   super-resolution flow fields are illustrated on the basis of two subsequent images, between which

198   the dynamics of structural features are apparent to the eye (Figure 4B-C). On the nuclear periphery,

199   connected regions spanning up to ~ 500 nm can be observed (Figure 4B (i-ii), marked by arrows).

200   These structures are stable for at least 360 ms but move from frame to frame. The flow field is

201   shown on top of an overlay of the two super-resolve images and color-coded (Figure 4B (iii), the

202   intensity in frame 1 is shown in green, the intensity in frame one is shown in purple, co-localization

203   of both is white). Displacement vectors closely follow the redistribution of intensity from frame to

204   frame (roughly from green to purple). Similarly, structures within the nuclear interior (Figure 4C)

205 can be followed by eye, thus further validating and justifying the use of a dense motion

206 reconstruction as a quantification tool of super-resolved chromatin motion.

207 Using Optical Flow fields, we linked the spatial appearance of chromatin to their dynamics.

208 Effectively, the blobs were characterized with two structural parameters (NND and area) and their

209 flow magnitude (Figure 4D). Supplementary Movie 1 shows the time evolution of those parameters

210 for an exemplary nucleus. Blobs at the nuclear periphery showed a distinct behavior from those in

211 the nuclear interior. In particular, the periphery exhibits a lower density of blobs, but those appear

212 slightly larger and are less mobile than in the nuclear interior (Supplementary Figure 7), in line with

213 previous findings using conventional microscopy (*26*).

214

215 **Chromatin structure and dynamics are linked**

216 To further elucidate the relationship between chromatin structure and dynamics, we analyzed the

217 correlations between each pair of parameters in space and time. Therefore, we computed the auto-

218 and cross-correlation of parameter maps with a given time lag across the entire nucleus (in space)

219 (Figure 5A). In general, a positive correlation denotes a low-low or a high-high relationship (a

220 variable de-/increases when another variable de-/increases) while analogously a negative

221 correlation denotes a high-low relationship. The autocorrelation of NND maps (Figure 5A(i)) shows

222 a positive correlation, thus regions exist spanning 2 - 4 μm, in which chromatin is either closely

223 packed (low-low) or widely dispersed (high-high). Likewise, blobs of similar size tend to be in

224 spatial proximity (Figure 5A(iii)). These regions are not stable over time but rearrange

225 continuously, an observation bolstered by the fact that the autocorrelation diminishes with

226 increasing time lag. The cross-correlation between NND and area (Figure 5A(ii)) shows a negative

227 correlation for short time lags, suggesting that large blobs appear with a high local density while

228 small ones are more isolated. Interestingly, the correlation becomes slightly positive for time lags

229 ≥ 20 s, indicating that big blobs are present in regions which were sparsely populated before and

230 small blobs tend to accumulate in previously densely populated regions. This is in line with dynamic

231 reorganization and reshaping of chromatin domains on a global scale as observed in snapshots of

232 the Deep-PALM image series (Figure 1A).

233 The flow magnitude is positively correlated for all time lags, while the correlation displays a slight

234 increase for time lags ≤ 20 s (Figure 5A(vi)), which has also been observed previously (*13, 25, 27*).

235 The spatial autocorrelation of dynamic and structural properties of chromatin are in stark contrast.

236 While structural parameters are highly correlated at short, but not at long time scales, chromatin

237 motion is still correlated at a time scale exceeding 30 s. At very short time scales (< 100 ms),

238 stochastic fluctuations determine the local motion of the chromatin fiber, while coherent motion

239 becomes apparent at longer times (*27*). However, there exists a strong cross-correlation between

240 structural and dynamic parameters: the cross-correlation between the NND and flow magnitude

241 shows striking negative correlation at all time lags (Figure 5A(iv)), strongly suggesting that sparsely

242 distributed blobs appear less mobile than densely packed ones. The area seems to play a negligible

243 role for short time lags, but there is a modest tendency that regions with large blobs tend to exhibit

244 increased dynamics at later time points (≥ 10 s; Figure 5A(v)), likely due to the strong relationship

245 between area and NND.

246 In general, parameter pairs involving chromatin dynamics exhibit an extended spatial auto- or cross-

247 correlation (up to ~ 6 μm; the lower row of Figure 5A), compared to correlation curves including

248 solely structural parameters (up to 3 - 4 μm). Furthermore, the cross-correlation of flow magnitude

249 and NND does not considerably change for increasing time lag, suggesting that the coupling

250 between those parameters is characterized by a surprisingly resilient memory, lasting for at least

251 tens of seconds (*28*). Concomitantly, the spatial correlation of time-averaged NND maps and maps

252 of the local diffusion constant of chromatin for the entire acquisition time enforce their negative

253 correlation at the time scale of ~ 1 min (Supplementary Figure 8). Such resilient memory was also

254 proposed by a computational study that observed that interphase nuclei behave like concentrated

255   solutions of unentangled ring polymers (*29*). Our data support the view that chromatin is mostly

256   unentangled since entanglement would influence the anomalous exponent of genomic loci in

257   regions of varying chromatin density (*29, 30*). However, our data do not reveal a correlation

258   between the anomalous exponent and the time-averaged chromatin density (Supplementary Figure

259   8), in line with our previous results using conventional microscopy (*26*).

260   Overall, the spatial cross-correlation between chromatin structure and dynamics indicates that the

261   NND between blobs and their mobility stand in a strong mutual, negative, relationship. This

262   relationship, however, concerns chromatin density variations at the nanoscale, but not global spatial

263   density variations such as in eu- or heterochromatin (*26*). These results support a model in which

264   regions with high local chromatin density, larger blobs are more prevalent and are mobile, while

265   small blobs are sparsely distributed and less mobile (Figure 5B). Blob density and dynamics in the

266   long-time limit are to a surprisingly large extent influenced by preceding chromatin conformations.

267

268   **The local chromatin density is a key regulator of instantaneous chromatin dynamics**

269   The spatial correlations above were only evaluated pairwise, while the behavior of every blob is

270   likely determined by a multitude of factors in the complex energy landscape of chromatin (*23, 27*).

271   Here, we aim to take a wider range of available information into account in order to reveal the

272   principle parameters, driving the observed chromatin structure and dynamics. Employing a

273   microscopy-based approach, we have access to a total of six relevant structural, dynamic and global

274   parameters, which potentially shape the chromatin landscape in space and time (Figure 6A). In

275   addition to the parameters used above, we included the confinement level as a relative measure,

276   allowing the quantification of transient confinement (Materials and Methods). We further included

277   the bare signal intensity of super-resolved images and, as the only static parameter, the distance

278   from the periphery since it was shown that dynamic and structural parameters show some

279   dependence on this parameter (Supplementary Figure 7). We then employed t-Distributed

280 Stochastic Neighbor Embedding (*31*) (t-SNE), a state of the art dimensionality reduction technique,

281 to map the six-dimensional chromatin 'features' (the six input parameters) into two dimensions.

282 (Figure 6A, see Supplementary Note 3). The t-SNE algorithm projects data points such that

283 neighbors in high-dimensional space likely stay neighbors in two-dimensional space (*31*). Visually

284 apparent grouping of points (Figure 6B) implies that grouped points exhibit great similarity with

285 respect to all input features and it is of interest to reveal which subset of the input features can

286 explain the similarity among chromatin blobs best. It is likely that points appear grouped because

287 their value of a certain input feature is considerably higher or lower than the corresponding value

288 of other data points. We hence labeled points in t-SNE maps which are smaller than the first quartile

289 point or larger than the third quartile point. Data points falling in either of the low/high partition of

290 one input feature are colored accordingly for visualization (Figure 6D; blue/red points respectively).

291 We then assigned a rank to each of the input features according to their nearest-neighbor fraction

292 (n-n fraction): Since the t-SNE algorithm conserves nearest neighbors, we described the extent of

293 grouping in t-SNE maps by the fraction of nearest neighbors which fall in either one of the

294 subpopulations of low or high points (illustrated in Supplementary Figure 9). A high nearest

295 neighbor fraction (n-n fraction; Figure 6C) therefore indicates that many points marked as low/high

296 are indeed grouped by t-SNE and are therefore similar. The ranking (from low to high n-n fraction)

297 reflects the potency of a given parameter to induce similar behavior between chromatin blobs with

298 respect to all input features.

299 The relative frequency at which each parameter ranked first provides an intuitive feeling for the

300 most 'influential' parameters in the dataset (Figure 6E). The signal intensity plays a negligible role,

301 suggesting that our data is free of potential artifacts related to the bare signal intensity. Furthermore,

302 the blob area and the distance from the periphery likewise do not considerably shape chromatin

303 blobs. In contrast, the NND between blobs was found to be the main factor inducing the observed

304 characteristics in 67 % of all-time frames across all nuclei. The flow magnitude and confinement

305 level together rank 1st in 26 % of all cases (11 % and 17 %, respectively). These numbers suggest

306 that the local chromatin density is a universal key regulator of instantaneous chromatin dynamics.

307 Note that no temporal dependency is included in the t-SNE analysis and thus the feature extraction

308 concerns only short-term (≤ 360 ms) relationships. The characteristics of roughly one-fourth of all

309 blobs at each time point are mainly determined by similar dynamical features. Mapping chromatin

310 blobs as marked in Figure 6C, D back to their respective positions inside the nucleus (Figure 6F)

311 shows that blobs with low/high flow magnitude or confinement level markedly also grouped in

312 physical space, which is highly reminiscent of coherent motion of chromatin (*25*). In contrast, blobs

313 with extraordinary low or high NND were found interspersed throughout the nucleus, in line with

314 spatial correlation analysis between structural and dynamic features (Figure 5). Our results point

315 towards a large influence of the local chromatin density on the dynamics of chromatin at the scale

316 of a few hundred nanometers and within a few hundred milliseconds. At longer time and length

317 scales, however, previous results suggest that this relationship is lost (*26*)

318

Discussion

319

320 With Deep-PALM we present temporally resolved super-resolution images of chromatin in living

321 cells. Our technique identified chromatin nanodomains, called "blobs", which mostly have an

322 elongated shape, consistent with the curvilinear arrangement of chromatin as revealed by Structured

323 Illumination Microscopy (*13*) with typical axes length of 45 – 90 nm. A previous study reported

324 ~30 nm wide 'clutches of nucleosomes' in fixed mammalian cells using STORM nanoscopy (*10*),

325 while the larger value obtained using Deep-PALM may be attributed to the motion blurring effect

326 in live-cell imaging. However, histone acetylation and methylation marks were shown to form

327 nanodomains of diameter 60 – 140 nm, respectively (*14*), which includes the computed dimensions

328 for histone H2B using Deep-PALM.

329 Using an established chromosome model, chromatin blobs were shown to consist of continuous

330 genomic regions with an average length of 75 kb. While assembling and disassembling dynamically

331 within less than one second. Monomers within blobs display a distinct TAD-like association pattern

332 in the long-time limit, suggesting that the identified blobs represent sub-TADs. Transient formation

333 is consistent with recent findings that TADs are not stable structural elements, but exhibit extensive

334 heterogeneity and dynamics (*7*, *9*).

335 We found that structural and dynamic parameters exhibit extended spatial and temporal (cross-)

336 correlations. Structural parameters such as the local chromatin density (expressed as the NND

337 between blobs) and area lose their correlation after $3 - 4$ μm and roughly 40 s in the spatial and

338 temporal dimension, respectively. In contrast, chromatin mobility correlations extend over ~ 6 μm

339 and persist during the whole acquisition period (≥ 40 s). Extensive spatio-temporal correlation of

340 chromatin dynamics have been presented previously, both experimentally (*25*) and in simulations

341 (*27*), but was not linked to the spatio-temporal behavior of the underlying chromatin structure until

342 now. We found that the chromatin dynamics are closely linked to the instantaneous, but also to past

343 local structural characterization of chromatin. In other words, the instantaneous local chromatin

344 density influences chromatin dynamics in the future and vice versa. Based on these findings, we

345 suggest that chromatin dynamics exhibit an extraordinary long memory. This strong temporal

346 relationship might be established by the fact that stress propagation is affected by the folded

347 chromosome organization (*32*). Fiber displacements cause structural reconfiguration, ultimately

348 leading to a local amplification of chromatin motion in local high-density environments. This

349 observation is also supported by the fact that increased nucleosome mobility grants chromatin

350 accessibility even within regions of high nucleosome density (*33*).

351 Given the persistence at which correlations of chromatin structure and, foremost, dynamics occur

352 in a spatio-temporal manner, we speculate that the interplay of chromatin structure and dynamics

353 could involve a functional relationship (*34*): transcriptional activity is closely linked to chromatin

354   accessibility and the epigenomic state (*35*). Because chromatin structure and dynamics are related,

355   dynamics could also correlate with transcriptional activity (*26*, *36*). However, it is currently

356   unknown if the structure-dynamics relationship revealed here is strictly mutual or if it may be

357   causal. Simulations hint that chromatin dynamics follows from structure (*27*, *28*), this question will

358   be exciting to answer experimentally and in the light of active chromatin remodelers in order to

359   elucidate a potential functional relationship to transcription. Chromatin regions which are switched

360   from inactive to actively transcribing, for instance, undergo a structural reorganization

361   accompanied by epigenetic modifications (*37*, *38*). The mechanisms driving recruitment of

362   enzymes inducing histone modifications such as histone acetyltransferases, deacetylases or

363   methyltransferases is largely unknown, but often involves the association to proteins (*39*). Their

364   accessibility to the chromatin fiber is inter alia determined by local dynamics (*33*). Such a structure-

365   dynamics feedback loop would constitute a quick and flexible way to transiently alter gene

366   expression patterns upon reaction to external stimuli or to co-regulate distant genes (*40*, *41*). Future

367   work will study how structure-dynamics correlations differ in regions of different transcriptional

368   activity and/or epigenomic states. Furthermore, to probe the interactions between key

369   transcriptional machines such as RNA polymerases with the local chromatin structure and to record

370   their (possibly collective) dynamics could shed light into the target search and binding mechanisms

371   of RNA polymerases with respect to the local chromatin structure. Deep-PALM in combination

372   with Optical Flow paves the way to answer these questions by enabling the analysis of time-

373   resolved super-resolution images of chromatin in living cells.

374

375

376

377

378

379   **Materials and Methods**

380   **Cell Culture.**

381   Human osteosarcoma U2OS expressing H2B-PATagRFP cells were a gift from Sébastien Huet

382   (CNRS, UMR 6290, Institut Génétique et Développement de Rennes, Rennes, France); the histone

383   H2B was cloned as described previously (*42*). U2OS cells were cultured in DMEM (with 4.5 g/l

384   glucose) supplemented with 10% fetal bovine serum (FBS), 2 mM glutamine, 100 μg/ml penicillin,

385   and 100 U/ml streptomycin in 5% CO_2 at 37°C. Cells were plated 24 hours before imaging on 35

386   mm Petri dishes with a #1.5 coverslip like bottom (ibidi, Biovalley) with a density of 2×10^5

387   cells/dish. Just before imaging, the growth medium was replaced by Leibovitz's L-15 medium (Life

388   Technologies) supplemented with 20% FBS, 2 mM glutamine, 100 μg/ml penicillin, and 100 U/ml

389   streptomycin.

390

391   **PALM Imaging.**

392   Imaging of H2B-PAtagRFP in live U2OS cells was carried out on a fully automated Nikon TI-E/B

393   PALM (Nikon Instruments) microscope. The microscope is equipped with a full incubator

394   enclosure with gas regulation to maintain a temperature of ~37°C for normal cell growth during

395   live-cell imaging. A laser line of 561 nm (~50-60 W/cm^2 at the sample) was applied for PATagRFP

396   excitation and the 405 nm laser used for photo-activation (~2-2.5 W/cm^2 at the sample). Laser beam

397   powers were controlled by acoustic optic-modulators (AA Opto-Electronics). Both wavelengths

398   were united into an oil immersion 1.49 NA TIRF objective (100x; Nikon). An oblique illumination

399   was applied to acquire image series with high signal to noise ratio. The fluorescence emission signal

400   was collected by using the same objective and spectrally filtered by a Quad-Band beam splitter

401   (ZT405/488/561/647rpc-UF2, Chroma Technology) with Quad-Band emission filter

402   (ZET405/488/561/647m-TRF, Chroma). The signal was recorded on an EMCCD camera (Andor

403   iXon X3 DU-897, Andor Technologies) with a pixel size of 108 nm. For axial correction, Perfect

404   Focus System was applied to correct for defocusing. NIS-Elements software was used for acquiring

405   the images at 30 ms per frame.

406

407   **Deep-PALM analysis.** The convolutional neural network (CNN) was trained using simulated data

408   following Nehme *et al.* (*19*) for three labeling densities (4, 6 and 9 emitters per μm^2 per frame).

409   Raw imaging data were checked for drift as previously described (*25*). The detected drift in raw

410   images is in the range < 10 nm and therefore negligible. The accuracy of the trained net was

411   evaluated by constructing ground truth images from the simulated emitter positions. The Structural

412   Similarity Index is computed to assess the similarity between reconstructed and ground truth images

413   (*43*):

$$SSIM = \sum_{x,y} \frac{(2\mu_x\mu_x + C_1)(2\sigma_{xy} + C_2)}{(\mu_x^2 + \mu_y^2 + C_1)(\sigma_x^2 + \sigma_y^2 + C_2)}, \tag{1}$$

414   where x and y are windows of the predicted and ground truth images, respectively, μ and σ denote

415   their local means and standard deviation, respectively and σ_{xy} their cross-variance. $C_1 = (0.01L)^2$

416   and $C_2 = (0.03L)^2$ are regularization constants, where L is the dynamic range of the input images.

417   The second quantity to assess CNN accuracy is the Root Mean Square Error between the ground

418   truth G and reconstructed image R:

419

$$RMSE = \sqrt{\frac{1}{N}\sum_{N}(R - G)^2}, \tag{2}$$

420

421   Where N is the number of pixels in the images. After training, experimental data were supplied

422   to the trained network and predictions of single Deep-PALM images were summed to a final super-

423   resolved image. An up-sampling factor of 8 was used, resulting in an effective pixel size of

424   108 nm/8 = 13.5 nm. The image quality assessment in order to determine the optimal number of

425   predictions to be summed, we use a blind/referenceless image spatial quality evaluator (BRISQUE)

426 (*44*). For visualization, super-resolved images were convolved with a Gaussian kernel ($\sigma = 1$

427 pixel) and represented using a false RGB colormap.

428

429 **Fourier Ring Correlation analysis.** Fourier Ring Correlation (FRC) is an unbiased method to

430 estimate the spatial resolution in microscopy images. We follow an approach similar to the one

431 described in Nieuwenhuizen *et al.* (*45*)*.* For localization-based super-resolution techniques, the set

432 of localizations is divided into two statistically independent subsets and two images from these

433 subsets are generated. The FRC is computed as the statistical correlation of the Fourier transforms

434 of both sub-images over the perimeter of circles of constant frequency in the frequency domain.

435 Deep-PALM, however, does not result in a list of localizations, but in predicted images directly.

436 The set of 12 predictions from Deep-PALM were thus split into two statistically independent

437 subsets and the method described in Nieuwenhuizen *et al.* (*45*) was applied.

438

439 **Chromatin blob identification.** The super-resolved images displayed isolated regions of

440 accumulated emitter density. To quantitatively assess the structural information implied by these

441 accumulation of emitters in the focal plane, we developed a segmentation scheme which aims to

442 identify individual blobs (Supplementary Figure 2). A marker-assisted watershed segmentation was

443 adapted in order to accurately determine blob boundaries. For this purpose, we use the raw

444 predictions from the deep convolutional neural network without convolution (Supplementary

445 Figure 2A). The foreground in this image is marked by regional maxima and pixels with very high

446 density (i.e. those with $I > 0.99\ I_{max}$, Supplementary Figure 2B). Since blobs are characterized by

447 surrounding pixels of considerably less density, the Euclidian distance transform is computed on

448 the binary foreground markers. Background pixels (i.e. those pixels not belonging to any blobs) are

449 expected to lie far away from any blob center and thus, a good estimate for background markers are

450 those pixels being furthest from any foreground pixel. We hence compute the watershed transform

451   on the distance transform of foreground markers and the resulting watershed lines depict

452   background pixels (Supplementary Figure 2C). Equipped with fore- and background markers

453   (Supplementary Figure 2D), we apply a marker-controlled watershed transform on the gradient of

454   the input image (Supplementary Figure 2E). The marker-controlled watershed imposes minima on

455   marker pixels preventing the formation of watershed lines across marker pixels. Therefore, the

456   marker-controlled watershed accurately detects boundaries as well as blobs which might not have

457   been previously marked as foreground (Supplementary Figure 2F). Finally, spurious blobs whose

458   median- or mean intensity is below 10% of the maximum intensity are discarded and each blob is

459   assigned a unique label for further correspondence (Supplementary Figure 2G). The area and

460   centroid position are computed for each identified blob for further analysis. This automated

461   segmentation scheme performs considerably better than other state-of-the-art algorithms for image

462   segmentation due to the reliable identification of fore- and background markers accompanied by

463   the watershed transform (Supplementary Note 1).

464

465   **Chromatin blob properties.** Centroid position, area, and eccentricity were computed. The

466   eccentricity is computed by describing the blobs as an ellipse:

$$E = \sqrt{1 - a^2/b^2} \tag{3}$$

467   where a and b are the short and long axes of the ellipse, respectively.

468

469   **Chromatin blob identification from a computational chromatin model.** We chose to employ a

470   computational chromatin model, recently introduced by Qi *et al.* (*23*)*,* in order to elucidate the

471   origin of experimentally determined chromatin blobs. Each bead of the model covers a sequence

472   length of 5 kb and is assigned one of 15 chromatin states to distinguish promoters, enhancers,

473   quiescent chromatin, etc. Starting from the simulated polymer configurations, we consider

474   monomers within a 200 nm thick slab through the center of the simulated chromosome. In order to

475 generate super-resolved images as those from Deep-PALM analysis, fluorescence intensity is

476 ascribed to each monomer. Monomer positions are subsequently discretized on a grid with 13.5 nm

477 spacing and convolved with a narrow point-spread function, which results in images closely

478 resembling experimental Deep-PALM images of chromatin. Chromatin blobs were then be

479 identified and characterized as on experimental data (Figure 2A, B). Mapping back the association

480 of each bead to a blob (if any) allows us to analyze principles of blob formation and maintenance

481 using the distance and the association strength between each pair of monomers, averaged over all

482 20,000 simulated polymer configurations.

483

484 **Radial distribution function.** The radial distribution function $g(r)$ (RDF, also pair correlation

485 function) is calculated (in two dimensions) by counting the number of blobs in an annulus of radius

486 r and thickness dr. The result is normalized by the bulk density $\rho = n/A$, with the total number of

487 blobs n and A the area of the nucleus, and the area of the annulus, $2\pi r \, dr$:

$$dn(r) = \rho \cdot g(r) \cdot 2\pi r \, dr \qquad (4)$$

488 **Quantification of chromatin dynamics.** Super-resolved images of chromatin showed spatially

489 distributed blobs of varying size, but the resolved structure is too dense for state-of-the-art single

490 particle tracking methods to track. Furthermore, are highly dynamic structures, assembling and

491 dissembling within $1 - 2$ super-resolved frames (Figure 3D), which makes a Single Particle

492 Tracking approach unsuitable. Instead, we used a method for dynamics reconstruction of bulk

493 macromolecules with dense labeling, Optical Flow. Optical Flow builds upon the computation of

494 flow fields between two successive frames of an image series. The integration of these flow fields

495 from super-resolution images results in trajectories displaying the local motion of bulk chromatin

496 with temporal and high spatial resolution. Further, the trajectories are classified into various

497 diffusion models and parameters describing the underlying motion are computed (*26*). Here, we use

498 the effective diffusion coefficient D (in units of m^2/s^α), which reflects the magnitude of

499 displacements between successive frames (the velocity of particles or monomers in the continuous

500 limit) and the anomalous exponent α (26). The anomalous exponent reflects if the diffusion is free

501 ($\alpha = 1$, e.g. for non-interacting particles in solution), directed ($\alpha > 1$, e.g. as the result from active

502 processes) or hindered ($\alpha < 1$, e.g. due to obstacles or an effective back-driving force).

503 Furthermore, we compute the length of constraint L_c which is defined as the standard deviation of

504 the trajectory positions with respect to its time-averaged position. Denoting $\boldsymbol{R}(t; \boldsymbol{R_0})$ the trajectory

505 at time t originating from $\boldsymbol{R_0}$, the expression reads (46) $L_c(\boldsymbol{R_0}) = var\big(\boldsymbol{R}(t; \boldsymbol{R_0})\big)^{1/2}$, where var

506 denotes the variance. The length of constraint is a measure of the length scale explored of the

507 monomer during the observation period. A complementary measure is the confinement level (47),

508 which computes the inverse of the variance of displacements within a sliding window of length ω:

509 $C \propto \omega / var\big(\boldsymbol{R}(t; \boldsymbol{R_0})\big)$, where the sliding window length is set to 4 frames (1.44 s). Larger values

510 of C denote a more confined state than small ones.

511

512 **Spatial correlation for temporally varying parameters.** The nearest-neighbor distance and the

513 area, as well as the flow magnitude, were calculated and assigned to the blobs' centroid position.

514 In order to calculate the spatial correlation between parameters, the parameters were interpolated

515 from the scattered centroid positions onto a regular grid spanning the entire nucleus. Because not

516 every pixel in the original super-resolved images is assigned a parameter value, we chose an

517 effective grid spacing of 5 pixels (67.5 nm) for the interpolated parameter maps. After interpolation,

518 the spatial correlation was computed between parameter pairs: Let $\boldsymbol{r} = (x, y)^T$ denote a position

519 on a regular two-dimensional grid and $f(\boldsymbol{r}, t)$ and $g(\boldsymbol{r}, t)$ two scalar fields with mean zero and

520 variance one, at time t on that grid. The time series of parameter fields consist of N time points.

521 The spatial cross-correlation between the fields f and g, which lie a lag time τ apart, is then

522 calculated as

$$C(\boldsymbol{\rho}, \tau) = \frac{1}{N} \sum_t \frac{\sum_{x,y} f(\boldsymbol{r}, t) g(\boldsymbol{r} + \boldsymbol{\rho}, t + \tau)}{\sum_{x,y} f(\boldsymbol{r}, t) \cdot g(\boldsymbol{r}, t + \tau)} \qquad (5)$$

523 where the space lag $\boldsymbol{\rho}$ is a two-dimensional vector $\boldsymbol{\rho} = (\Delta x, \Delta y)^T$. The sums in the numerator and

524 denominator are taken over the spatial dimensions, the first sum is taken over time. The average is

525 thus taken over all time points which are compliant with time lag τ. Subsequently, the radial average

526 in space is taken over the correlation, thus effectively calculating the spatial correlation $C(\rho, \tau)$

527 over the space lag $\rho = \sqrt{\Delta x^2 + \Delta y^2}$. If $f = g$, the spatial autocorrelation is computed.

528

529 **Spatial correlation for static parameters.** We denote global parameters as those, which reflect

530 the structural and dynamic behavior of chromatin spatially resolved, but in a time-averaged manner.

531 Examples involve the diffusion constant, the anomalous exponent, the length of constraint, but also

532 time-averaged nearest-neighbor distance maps, etc. (Supplementary Figure 8). Those parameters

533 are useful to determine time-universal characteristics. The spatial correlation between those

534 parameters is equivalent to the expression given for temporally varying parameters when the

535 temporal dimension is omitted, effectively resulting in a correlation curve $C(\rho)$.

536

537 **t-Distributed Stochastic Neighbor Embedding (t-SNE).** The distance from the periphery,

538 intensity, their nearest-neighbor distance, area, flow magnitude and confinement level of each

539 identified blob form the six-dimensional input feature space for t-SNE analysis. The parameters for

540 each blob (n = 3,260,232, divided into subsets of approximately 10,000) were z-transformed prior

541 to the t-SNE analysis. The t-SNE analysis was performed using MATLAB and the Statistics and

542 Machine Learning Toolbox (Release 2017b, The MathWorks, Inc., Natick, Massachusetts, United

543 States) with the Barnes-Hut approximation. The algorithm was tested using different distance

544 metrics and perplexity values and showed robust results within the examined ranges

545 (Supplementary Note 3, Supplementary Figure 10).

546

547 **H2: Supplementary Materials**

548

549 Note S1. Performance of the segmentation scheme employed for this study in comparison to other

550 state-of-the-art algorithms for general purpose and comparison of blob segmentation on

551 experimental images and on images containing randomly distributed emitters.

552 Note S2. Suitability of Optical Flow for super-resolution images of chromatin.

553 Note S3. t-SNE and its robustness with respect to distance metrics and perplexity values.

554 Figure S1. CNN training and time-resolution determination.

555 Figure S2. Chromatin blob identification pipeline.

556 Figure S3. Performance of segmentation algorithms on super-resolved images of chromatin *in vivo*.

557 Figure S4. Segmentation on images of randomly distributed emitters.

558 Figure S5. Chromatin area fraction.

559 Figure S6. Performance of Optical Flow on conventional and super-resolved images.

560 Figure S7. Structural and dynamic parameters are dependent on the proximity to the nuclear

561 periphery.

562 Figure S8. Global spatial correlation of structural and dynamic parameters.

563 Figure S9. Clustering illustration of points within a subset based on nearest-neighbors in t-SNE

564 maps.

565 Figure S10. t-SNE for different distance metrics and perplexity values.

566 Movie S1. Time series of super-resolved chromatin structure and dynamics.

567

568 **References and Notes**

569 1.   J. H. Gibcus, J. Dekker, The Hierarchy of the 3D Genome. *Mol. Cell*. **49** (2013), pp. 773–

570   782.

571 2.   W. A. Bickmore, The spatial organization of the human genome. *Annu Rev Genomics Hum*

Genet. **14**, 67–84 (2013).

3.   B. van Steensel, E. E. M. Furlong, The role of transcription in shaping the spatial organization of the genome. *Nat. Rev. Mol. Cell Biol.* (2019), , doi:10.1038/s41580-019-0114-6.

4.   E. Lieberman-Aiden, N. L. van Berkum, L. Williams, M. Imakaev, T. Ragoczy, A. Telling, I. Amit, B. R. Lajoie, P. J. Sabo, M. O. Dorschner, R. Sandstrom, B. Bernstein, M. A. Bender, M. Groudine, A. Gnirke, J. Stamatoyannopoulos, L. A. Mirny, E. S. Lander, J. Dekker, N. L. Van Berkum, L. Williams, M. Imakaev, T. Ragoczy, A. Telling, I. Amit, B. R. Lajoie, P. J. Sabo, M. O. Dorschner, R. Sandstrom, B. Bernstein, M. A. Bender, M. Groudine, A. Gnirke, J. Stamatoyannopoulos, L. A. Mirny, Comprehensive Mapping of Long-Range Interactions Reveals Folding Principles of the Human Genome. *Science (80-.).* **326**, 289–293 (2009).

5.   A. Bolzer, G. Kreth, I. Solovei, D. Koehler, K. Saracoglu, C. Fauth, S. M??ller, R. Eils, C. Cremer, M. R. Speicher, T. Cremer, Three-dimensional maps of all chromosomes in human male fibroblast nuclei and prometaphase rosettes. *PLoS Biol.* **3**, 0826–0842 (2005).

6.   J. R. Dixon, S. Selvaraj, F. Yue, A. Kim, Y. Li, Y. Shen, M. Hu, J. S. Liu, B. Ren, Topological domains in mammalian genomes identified by analysis of chromatin interactions. *Nature*. **485**, 376–380 (2012).

7.   B. Bintu, L. J. Mateo, J.-H. Su, N. A. Sinnott-Armstrong, M. Parker, S. Kinrot, K. Yamaya, A. N. Boettiger, X. Zhuang, Super-resolution chromatin tracing reveals domains and cooperative interactions in single cells. *Science (80-.).* **362**, eaau1783 (2018).

8.   M. Spielmann, D. G. Lupiáñez, S. Mundlos, Structural variation in the 3D genome. *Nat. Rev. Genet.* **19**, 453–467 (2018).

9.   E. H. Finn, G. Pegoraro, H. B. Brandão, A. L. Valton, M. E. Oomen, J. Dekker, L. Mirny, T. Misteli, Extensive Heterogeneity and Intrinsic Variation in Spatial Genome

597   Organization. *Cell*. **176**, 1502-1515.e10 (2019).

598   10.   M. A. Ricci, C. Manzo, M. F. García-Parajo, M. Lakadamyali, M. P. Cosma, Chromatin

599   fibers are formed by heterogeneous groups of nucleosomes in vivo. *Cell* (2015),

600   doi:10.1016/j.cell.2015.01.054.

601   11.   B. Dong, L. M. Almassalha, Y. Stypula-Cyru, B. E. Urban, J. E. Chandler, T. Q. Nguyen,

602   C. Sun, H. F. Zhang, V. Backman, Superresolution intrinsic fluorescence imaging of

603   chromatin utilizing native, unmodified nucleic acids for contrast. *Proc. Natl. Acad. Sci. U.*

604   *S. A.* (2016), doi:10.1073/pnas.1602202113.

605   12.   K. Fang, X. Chen, X. Li, Y. Shen, J. Sun, D. M. Czajkowsky, Z. Shao, Super-resolution

606   Imaging of Individual Human Subchromosomal Regions in Situ Reveals Nanoscopic

607   Building Blocks of Higher-Order Structure. *ACS Nano* (2018),

608   doi:10.1021/acsnano.8b01963.

609   13.   E. Miron, R. Oldenkamp, D. M. S. Pinto, J. M. Brown, A. R. Faria, H. A. Shaban, J. D. P.

610   Rhodes, C. Innocent, S. de Ornellas, V. Buckle, L. Schermelleh, Chromatin arranges in

611   filaments of blobs with nanoscale functional zonation. *bioRxiv*, 566638 (2019).

612   14.   J. Xu, H. Ma, J. Jin, S. Uttam, R. Fu, Y. Huang, Y. Liu, H. Ma, J. Jin, S. Uttam, R. Fu, Y.

613   Huang, Y. Liu, Super-Resolution Imaging of Higher-Order Chromatin Structures at

614   Different Epigenomic States in Single Mammalian Cells. *Cell Rep.* **24** (2018),

615   doi:10.1016/j.celrep.2018.06.085.

616   15.   A. N. Boettiger, B. Bintu, J. R. Moffitt, S. Wang, B. J. Beliveau, G. Fudenberg, M.

617   Imakaev, L. A. Mirny, C. T. Wu, X. Zhuang, Super-resolution imaging reveals distinct

618   chromatin folding for different epigenetic states. *Nature*. **529**, 418–422 (2016).

619   16.   T. Nozaki, R. Imai, M. Tanbo, R. Nagashima, S. Tamura, T. Tani, Y. Joti, M. Tomita, K.

620   Hibino, M. T. Kanemaki, K. S. Wendt, Y. Okada, T. Nagai, K. Maeshima, Dynamic

621   Organization of Chromatin Domains Revealed by Super-Resolution Live-Cell Imaging.

622 *Mol. Cell*. **67**, 282-293.e7 (2017).

17. H. A. Shaban, R. Barth, K. Bystricky, Formation of correlated chromatin domains at nanoscale dynamic resolution during transcription. *Nucleic Acids Res.* **46**, e77–e77 (2018).

18. W. Xiang, M. J. Roberti, J.-K. Hériché, S. Huet, S. Alexander, J. Ellenberg, Correlative live and super-resolution imaging reveals the dynamic structure of replication domains. *J. Cell Biol.* **217**, 1973–1984 (2018).

19. E. Nehme, L. E. Weiss, T. Michaeli, Y. Shechtman, Deep-STORM: super-resolution single-molecule microscopy by deep learning. *Optica*. **5**, 458 (2018).

20. H. Shroff, C. G. Galbraith, J. A. Galbraith, E. Betzig, Live-cell photoactivated localization microscopy of nanoscale adhesion dynamics. *Nat. Methods* (2008), doi:10.1038/nmeth.1202.

21. Q. Szabo, D. Jost, J.-M. M. Chang, D. I. Cattoni, G. L. Papadopoulos, B. Bonev, T. Sexton, J. Gurgo, C. Jacquier, M. Nollmann, F. Bantignies, G. Cavalli, G. L. Papadopoulos, Q. Szabo, B. Bonev, D. Jost, F. Bantignies, C. Jacquier, D. I. Cattoni, J. Gurgo, M. Nollmann, J.-M. M. Chang, G. Cavalli, TADs are 3D structural units of higher-order chromosome organization in Drosophila . *Sci. Adv.* **4**, eaar8082 (2018).

22. R. J. Marsh, K. Pfisterer, P. Bennett, L. M. Hirvonen, M. Gautel, G. E. Jones, S. Cox, Artifact-free high-density localization microscopy analysis. *Nat. Methods*. **15**, 689–692 (2018).

23. Y. Qi, B. Zhang, Predicting three-dimensional genome organization with chromatin states. *PLOS Comput. Biol.* **15**, e1007024 (2019).

24. H. D. Ou, S. Phan, T. J. Deerinck, A. Thor, M. H. Ellisman, C. C. O'Shea, ChromEMT: Visualizing 3D chromatin structure and compaction in interphase and mitotic cells. *Science (80-.).* **357** (2017), doi:10.1126/science.aag0025.

25. H. A. Shaban, R. Barth, K. Bystricky, Formation of correlated chromatin domains at

647   nanoscale dynamic resolution during transcription. *Nucleic Acids Res.* **46**, e77–e77 (2018).

648   26.   H. A. Shaban, R. Barth, K. Bystricky, Nanoscale mapping of DNA dynamics in live human

649   cells. *Bioarxiv* (2018).

650   27.   M. Di Pierro, D. A. Potoyan, P. G. Wolynes, J. N. Onuchic, Anomalous diffusion, spatial

651   coherence, and viscoelasticity from the energy landscape of human chromosomes. *Proc.*

652   *Natl. Acad. Sci.* **115**, 7753–7758 (2018).

653   28.   L. Liu, G. Shi, D. Thirumalai, C. Hyeon, Chain organization of human interphase

654   chromosome determines the spatiotemporal dynamics of chromatin loci. *PLOS Comput.*

655   *Biol.* **14**, e1006617 (2018).

656   29.   A. Rosa, R. Everaers, Structure and Dynamics of Interphase Chromosomes. *PLoS Comput.*

657   *Biol.* **4**, e1000153 (2008).

658   30.   P. G. de Gennes, L. Leger, Dynamics of Entangled Polymer Chains. *Annu. Rev. Phys.*

659   *Chem.* **33**, 49–61 (1982).

660   31.   L. Van Der Maaten, G. Hinton, Visualizing Data using t-SNE. **9**, 2579–2605 (2008).

661   32.   K. E. Polovnikov, M. Gherardi, M. Cosentino-Lagomarsino, M. V. Tamm, Fractal Folding

662   and Medium Viscoelasticity Contribute Jointly to Chromosome Dynamics. *Phys. Rev. Lett.*

663   **120**, 88101 (2018).

664   33.   S. Hihara, C.-G. G. Pack, K. Kaizu, T. Tani, T. Hanafusa, T. Nozaki, S. Takemoto, T.

665   Yoshimi, H. Yokota, N. Imamoto, Y. Sako, M. Kinjo, K. Takahashi, T. Nagai, K.

666   Maeshima, Local Nucleosome Dynamics Facilitate Chromatin Accessibility in Living

667   Mammalian Cells. *Cell Rep.* **2**, 1645–1656 (2012).

668   34.   L. Giorgetti, R. Galupa, E. P. Nora, T. Piolot, F. Lam, J. Dekker, G. Tiana, E. Heard,

669   Predictive polymer modeling reveals coupled fluctuations in chromosome conformation

670   and transcription. *Cell*. **157**, 950–963 (2014).

671   35.   S. M. Gorisch, Histone acetylation increases chromatin accessibility. *J. Cell Sci.* **118**,

672   5825–5834 (2005).

673   36.   T. Germier, S. Kocanova, N. Walther, A. Bancaud, H. A. Shaban, H. Sellou, A. Z. Politi, J.

674   Ellenberg, F. Gallardo, K. Bystricky, Real-Time Imaging of a Single Gene Reveals

675   Transcription-Initiated Local Confinement. *Biophys. J.* **113**, 1383–1394 (2017).

676   37.   N. Soshnikova, D. Duboule, Epigenetic Temporal Control of Mouse Hox Genes in Vivo.

677   *Science (80-.).* **324**, 1320–1323 (2009).

678   38.   D. Noordermeer, M. Leleu, E. Splinter, J. Rougemont, W. De Laat, D. Duboule, The

679   Dynamic Architecture of Hox Gene Clusters. *Science (80-.).* **334**, 222–225 (2011).

680   39.   M. Laisné, N. Gupta, O. Kirsh, S. Pradhan, P.-A. Defossez, Mechanisms of DNA

681   Methyltransferase Recruitment in Mammals. *Genes (Basel).* **9**, 617 (2018).

682   40.   P. Fraser, W. Bickmore, Nuclear organization of the genome and the potential for gene

683   regulation. *Nature*. **447**, 413–417 (2007).

684   41.   G. Fourel, F. Magdinier, É. Gilson, Insulator dynamics and the setting of chromatin

685   domains. *BioEssays*. **26**, 523–532 (2004).

686   42.   H. Sellou, T. Lebeaupin, C. Chapuis, R. Smith, A. Hegele, H. R. Singh, M. Kozlowski, S.

687   Bultmann, A. G. Ladurner, G. Timinszky, S. Huet, The poly(ADP-ribose)-dependent

688   chromatin remodeler Alc1 induces local chromatin relaxation upon DNA damage. *Mol.*

689   *Biol. Cell*. **27**, 3791–3799 (2016).

690   43.   Z. Wang, A. C. Bovik, H. R. Sheikh, E. P. Simoncelli, Image quality assessment: From

691   error visibility to structural similarity. *IEEE Trans. Image Process.* (2004),

692   doi:10.1109/TIP.2003.819861.

693   44.   A. Mittal, A. K. Moorthy, A. C. Bovik, No-Reference Image Quality Assessment in the

694   Spatial Domain. *IEEE Trans. Image Process.* **21**, 4695–4708 (2012).

695   45.   R. P. J. Nieuwenhuizen, K. A. Lidke, M. Bates, D. L. Puig, D. Grünwald, S. Stallinga, B.

696   Rieger, Measuring image resolution in optical nanoscopy. *Nat. Methods* (2013),

697   doi:10.1038/nmeth.2448.

698   46.   A. Amitai, A. Seeber, S. M. Gasser, D. Holcman, Visualization of Chromatin

699   Decompaction and Break Site Extrusion as Predicted by Statistical Polymer Modeling of

700   Single-Locus Trajectories. *Cell Rep.* **18**, 1200–1214 (2017).

701   47.   A. Sergé, N. Bertaux, H. Rigneault, D. Marguet, A. Sergé, N. Bertaux, H. Rigneault, D.

702   Marguet, Dynamic multiple-target tracing to probe spatiotemporal cartography of cell

703   membranes. *Nat. Methods*. **5**, 687–694 (2008).

704   48.   S. S. P. Rao, M. H. Huntley, N. C. Durand, E. K. Stamenova, I. D. Bochkov, J. T.

705   Robinson, A. L. Sanborn, I. Machol, A. D. Omer, E. S. Lander, E. L. Aiden, A 3D map of

706   the human genome at kilobase resolution reveals principles of chromatin looping. *Cell*.

707   **159**, 1665–1680 (2014).

708   49.   S. Beucher, B. Marcotegui, B. P. Marcotegui, "P algorithm, a dramatic enhancement of the

709   waterfall transformation" (2009), (available at http://cmm.ensmp.fr/beucher/publi/).

710   50.   W. M. Rand, Objective Criteria for the Evaluation of Clustering Methods. *J. Am. Stat.*

711   *Assoc.* **66**, 846 (1971).

712

713   **Acknowledgments**

714

721

722 **Author contributions:** H.A.S. designed and supervised the project; R.B. designed the data analysis

723 and wrote the code, H.A.S carried out experimental work; R.B. carried out the data analysis; H.A.S.

724 and R. B interpreted results: H.A.S, R.B. and K.B. wrote the manuscript.

725

726 **Competing interests:** The authors declare no competing financial interest.

727

728 **Data and materials availability:** All data needed to evaluate the conclusions in the paper are

729 present in the paper and/or the Supplementary Materials. Additional data related to this paper may

730 be requested from the authors.

731

732 **Figures and Tables**

733 **Figure 1: Temporally resolved super-resolution images of chromatin in U2OS nuclei. A)**

734 Widefield images of U2OS nuclei expressing H2B-PATagRFP are input to a trained convolutional

735 neural network (CNN) and predictions from multiple input frames are summed to construct a super-

736 resolved image of chromatin *in vivo*. **B)** The resolution tradeoff between the prolonged acquisition

737 of emitter localizations (green line) and motion blur due to diffusion of the underlying diffusion

738 processes (purple line). For our experimental data, the localization density per second is $\rho =$

739 $(2.4 \pm 0.1)\ \mu m^{-2} s^{-1}$, the diffusion constant is $D = (3.4 \pm 0.8) \cdot 10^{-3}\ \mu m^2 s^{-1}$ (see

740 Supplementary Figure 8B) and the acquisition time per frame is $\tau = 30\ ms$. The spatial resolution

741 assumes a minimum $(69 \pm 5\ nm)$ at a time resolution of 360 ms. **C)** Super-resolution images of a

742 single nucleus at time intervals of about 10 seconds. Scale bar is 2 µm. **D)** Magnification of

743 segregated accumulations of H2B within a chromatin-rich region. Scale bar is 200 nm. **E)**

744 Magnification of a stable, but dynamic structure (arrows) over three consecutive images. Scale bar

745 is 500 nm. **F)** Fourier Ring Correlation (FRC) for super-resolved images resulting in a spatial

746 resolution of 63 ± 2 nm.

747

Figure 2: Chromatin blob identification and characterization of imaged and modeled chromatin. A) Super-resolved images show blobs of chromatin (left). These blobs are segmented (Materials and Methods, Supplementary Note 1) and individually labeled by random color (right). Magnifications of the boxed regions are shown. Scale bars: whole nucleus 2 μm, magnifications 200 nm. **B)** Generation of super-resolution images and blob identification and characterization for a 25 Mbp segment of chromosome 1 from GM12878 cells as simulated in Qi *et al.* (*23*). Beads (5 kb genomic length) of a simulated polymer configuration within a 200 nm thick slab are projected to the imaging plane, resembling experimental super-resolved images of live chromatin. Blobs are identified as on experimental data. **C)** From the centroid positions, the nearest-neighbor distance (NND) distributions are computed for up to 40 nearest neighbors (blue to red). The envelope of the k-NND distributions (black line) shows peaks at approximately 95 nm, 235 nm, 335 nm and 450 nm (red dots). **D)** k-NND distributions as in B) for simulated data. **E)** Area distribution of experimental and simulated blobs. The distribution is in both cases well described by a lognormal distribution with parameters $(\mathbf{3.3 \pm 2.8}) \cdot \mathbf{10^{-3}}$ μm^2 for experimental blobs and $(\mathbf{3.1 \pm 3.2}) \cdot \mathbf{10^{-3}}$ μm^2 for simulated blobs (mean $\pm$ standard deviation). **F)** Eccentricity distribution for experimental and simulated chromatin blobs. Selected eccentricity values are illustrated by ellipses with the corresponding eccentricity. Eccentricity values range from 0, describing a circle, to 1, describing a line. Prominent peaks arise due to the discretization of chromatin blobs in pixels.

Figure 3: Chromatin blobs on modeled chromosomes consist of continuous loci along the genome and exhibit a TAD-like time-averaged conformation. A) Gap length between beads belonging to the same blob. An exemplary blob with small gap length is shown. The blob is mostly made of consecutive beads being in close spatial proximity. **B)** A representative polymer configuration is colored according to chromatin states (red: active, green: inactive, blue: repressive). **C)** The cumulative distribution function of clusters within active, inactive and

772 repressive chromatin. Inset: Mean area of clusters within the three types of chromatin. The

773 distributions are all significantly different from each other as determined by a two-sample

774 Kolmogorov-Smirnov test (p $< 10^{-50}$). **D)** Distribution of the continuous residence time of any

775 monomer within a cluster (0.5 $\pm$ 0.3 s; mean $\pm$ standard deviation). Inset: Continuous residence

776 time of any monomer within a slab of 200 nm thickness (1.5 $\pm$ 1.6 s; mean $\pm$ standard deviation).

777 **E)** The blob association strength between any two beads is measured as the frequency at which any

778 two beads are found in one blob. The association map is averaged over all simulated configurations

779 (upper triangular matrix; from simulations) and experimental Hi-C counts are shown for the same

780 chromosome segment (lower triangular matrix; from Rao *et al.* (*48*)). The association and Hi-C

781 maps are strongly correlated (Pearson's correlation coefficient PCC = 0.76) **F)** Close-up views

782 around the diagonal of Hi-C-like matrices. The association strength is shown together with the

783 inverse distance between beads (upper panel; PCC = 0.85) and with experimental Hi-C counts

784 (lower panel; as in E)).

785

786 **Figure 4: Super-resolution chromatin dynamics. A)** A time series of super-resolution images

787 (left panel) is subject to Optical Flow (right panel). **B)** (i-ii) Two subsequent images of chromatin.

788 Magnifications show prominent mobile blobs on the nuclear periphery in both images (colored

789 arrows). (iii) The flow field and corresponding magnification are shown on top of a fused image of

790 both super-resolved images in (i) and (ii) (green and purple respectively, co-localization are white).

791 The flow field is colored according to the direction of vectors (see color wheel) **C)** As for B) in the

792 nuclear interior. Scale bars: whole nucleus 2 µm, magnifications 500 nm. Flow vectors are not

793 drawn to scale and down-sampled 8-fold for clarity. **D)** Blobs of a representative nucleus (see

794 Supplementary Movie 1) are labeled by their NND (left), area (middle) and flow magnitude (right).

795 Colors denote the corresponding parameter magnitude.

796

797   **Figure 5: Spatio-temporal correlations between structural and dynamic parameters. A)** The

798   spatial auto- and cross-correlation between parameters were computed for different time lags. The

799   graphs depict the correlation over space lag for each parameter pair and different colors denote the

800   time lag (increasing from blue to red). **B)** Illustration of the instantaneous relationship between local

801   chromatin density and dynamics. The blob density is shown in blue; the magnitude of chromatin

802   dynamics is shown by red arrows. The consistent negative correlation between NND and flow

803   magnitude is expressed by increased dynamics in regions of high local blob density.

804   **Figure 6: Chromatin feature extraction. A)** The six-dimensional parameter space is input to the

805   t-SNE algorithm and projected to two dimensions. **B)** The 2D embedding of an exemplary data set

806   is shown and colored according to the magnitude of each input feature (blue to red, the parameter

807   average is shown in beige) **C)** Points below the first (blue) and above the third (red) quartile points

808   of the corresponding parameter are marked and the parameters are ranked according to the fraction

809   of nearest neighbors which fall in one of the marked regions. **D)** Data points marked below the first

810   or above the third quartile points are labeled according to the feature in which they were marked.

811   Priority is given to the feature with the higher nearest-neighbor fraction if necessary. **E)** t-SNE

812   analysis is carried out for each nucleus over the whole time series and it is counted how often a

813   parameter ranked 1st. The results are visualized as a pie chart. The NND predominantly ranks 1st in

814   about 2/3 of all cases. **F)** Marked points in C-D) are mapped back onto the corresponding nuclei

815   and the cumulative distribution function (CDF) over space is shown.

816

817

818

819 **Figure 1**
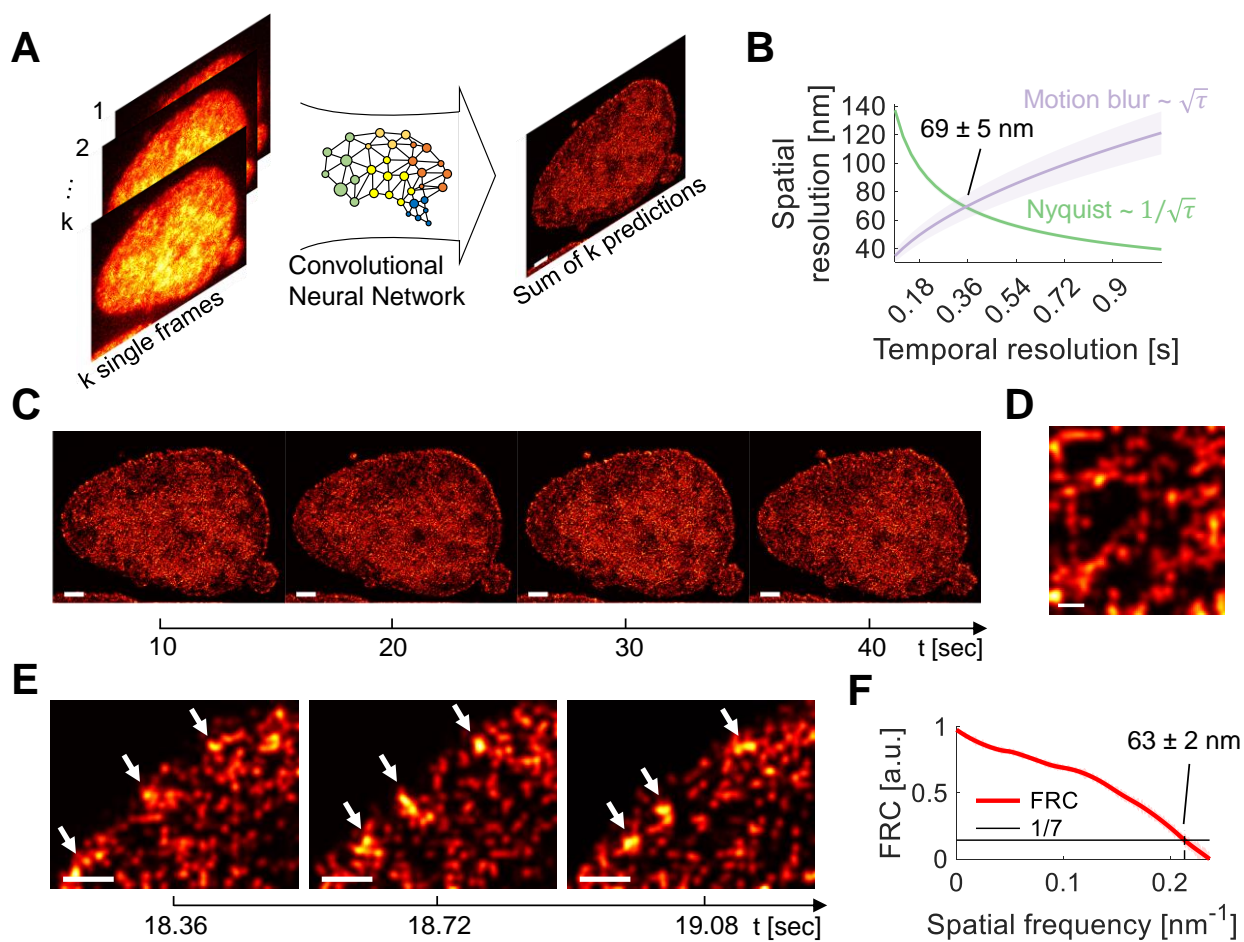
821   **Figure 2**
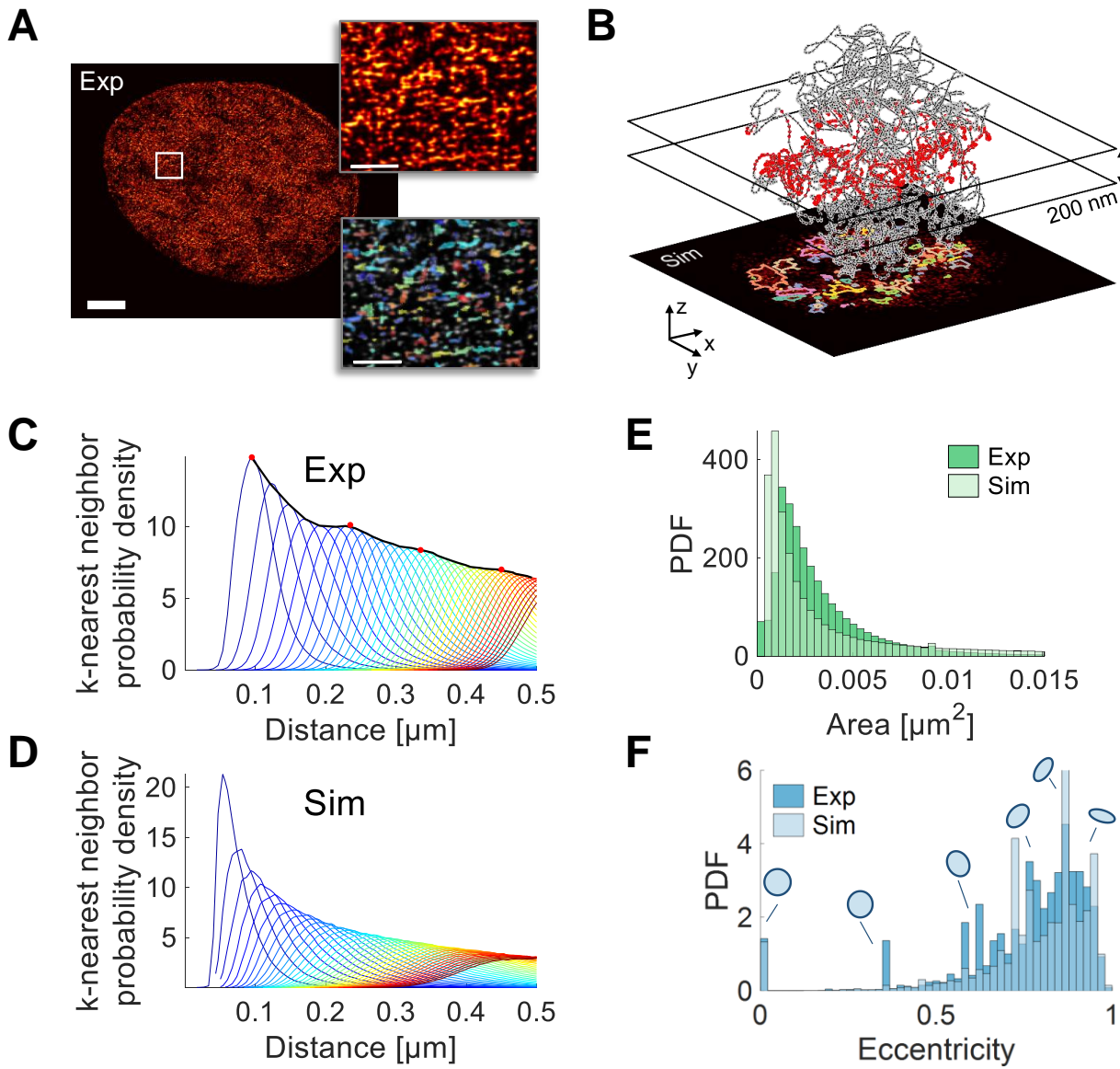
822

823   **Figure 3**
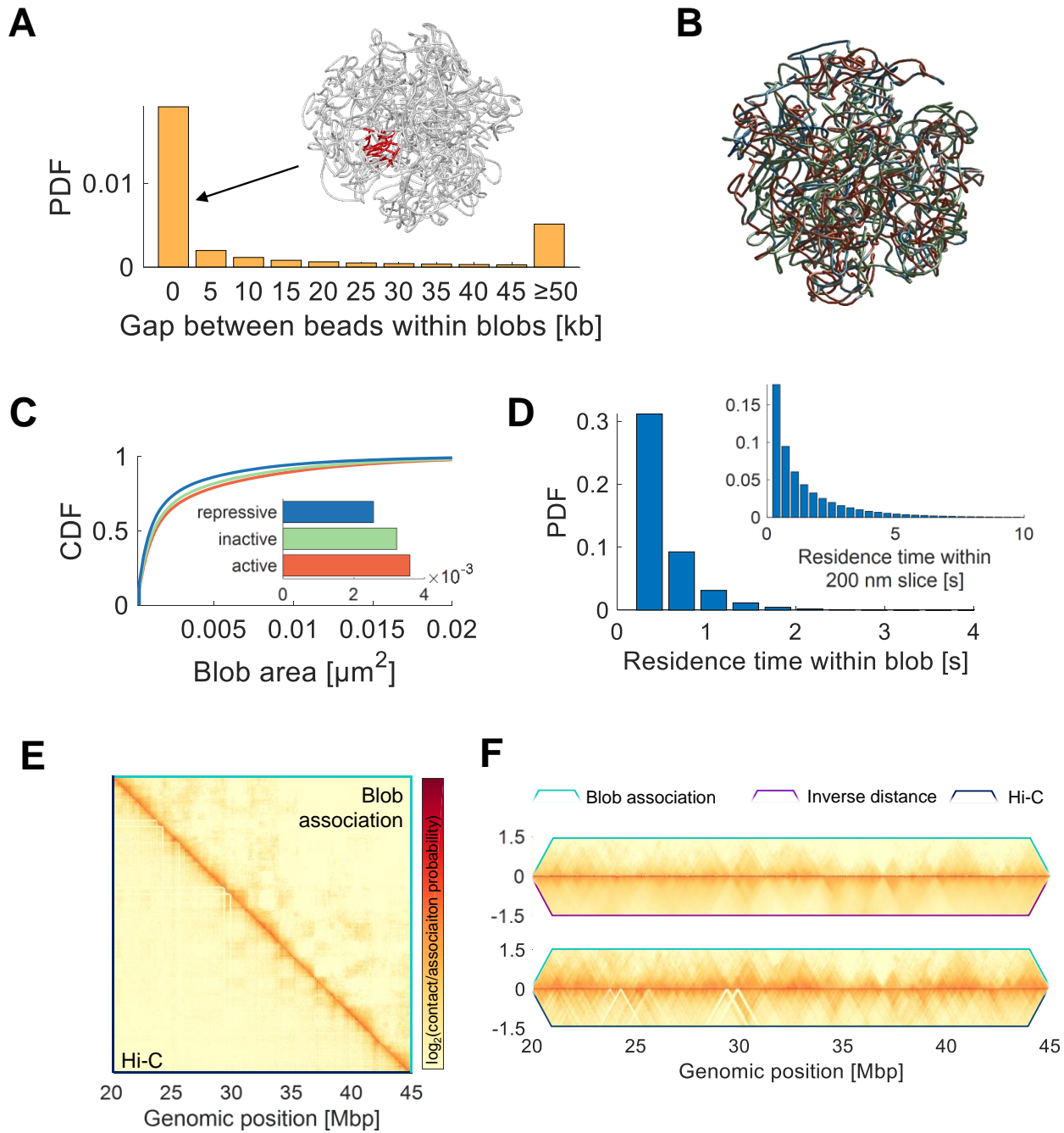
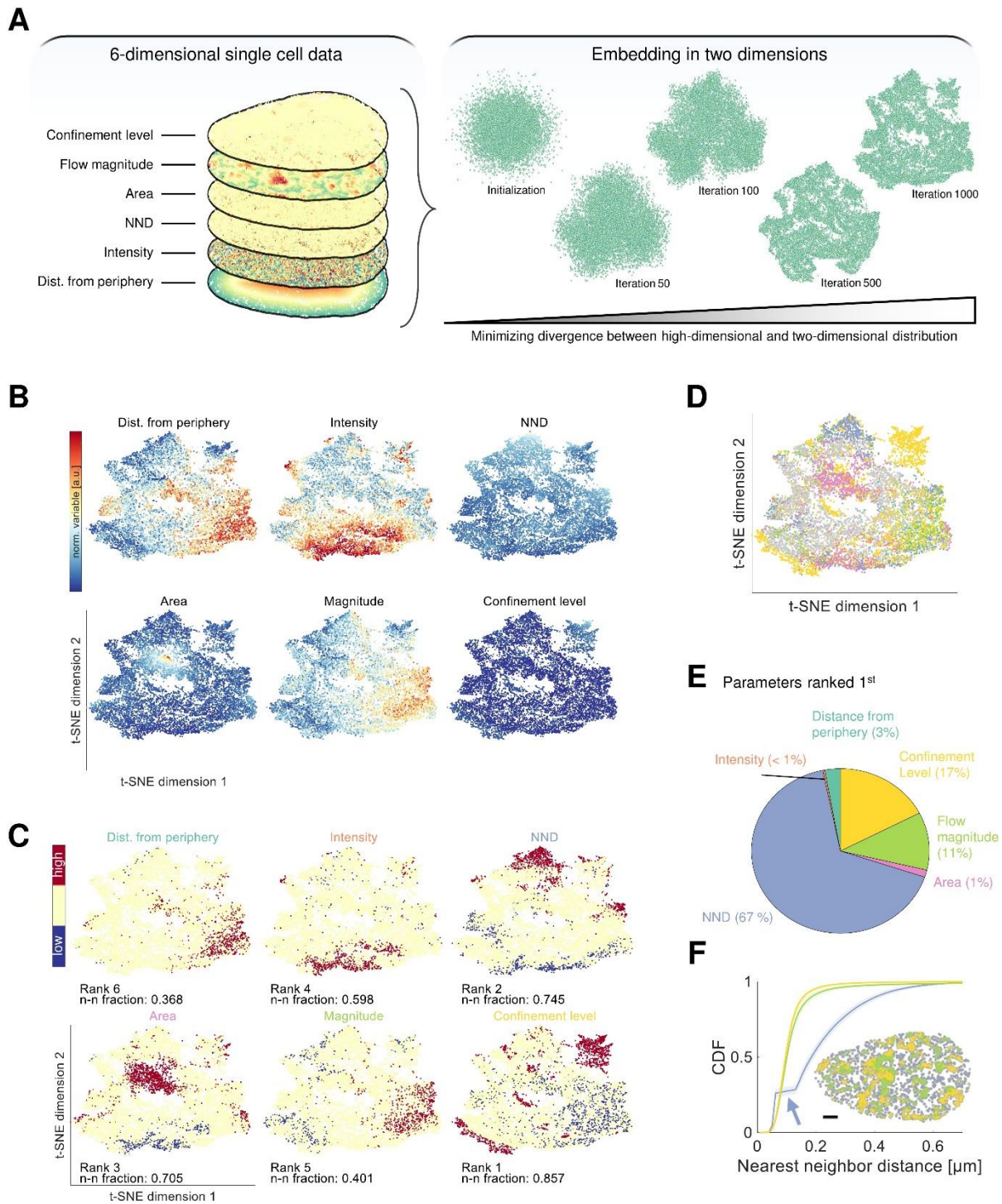

824

825   **Figure 4**

826

827 **Figure 5**

828

829
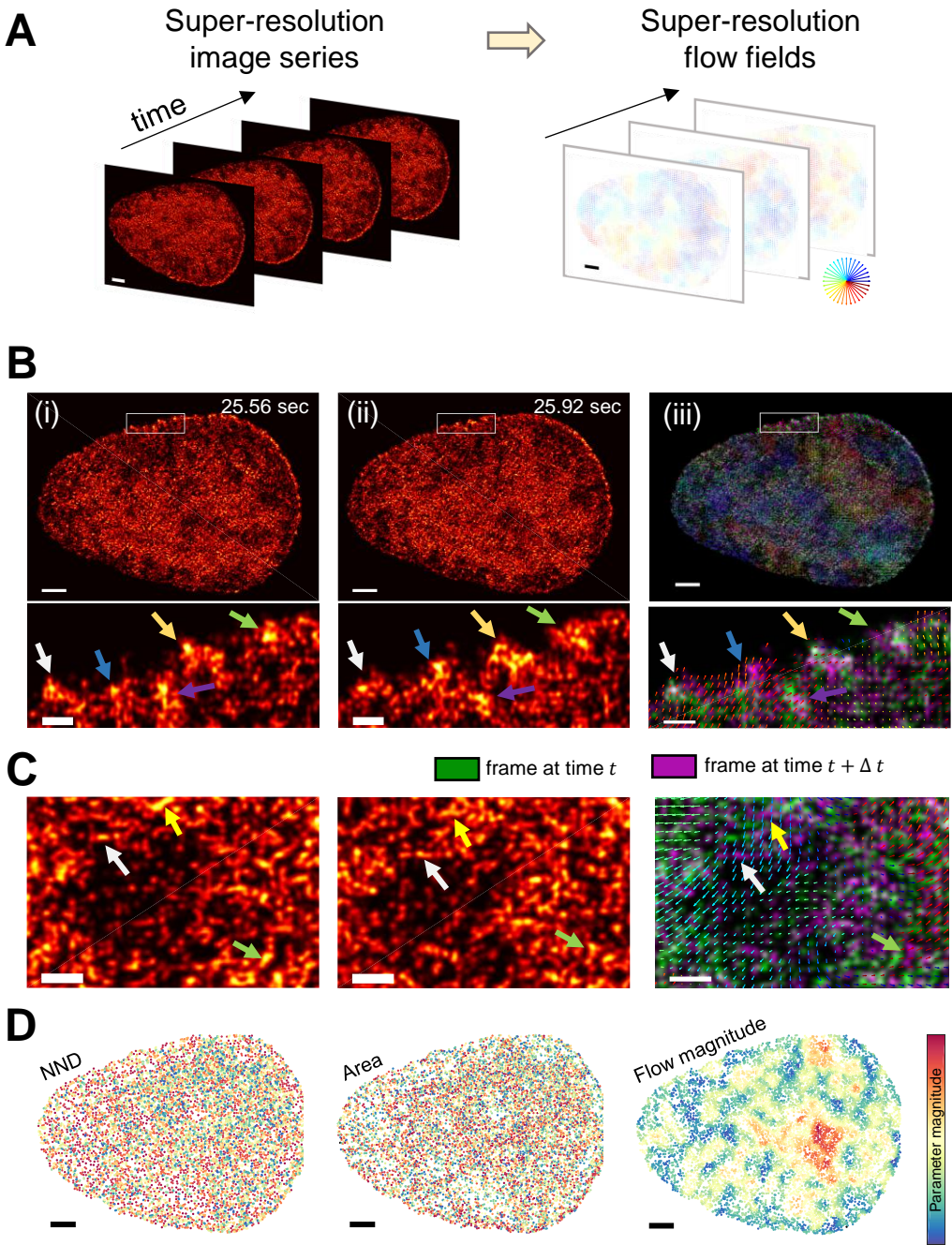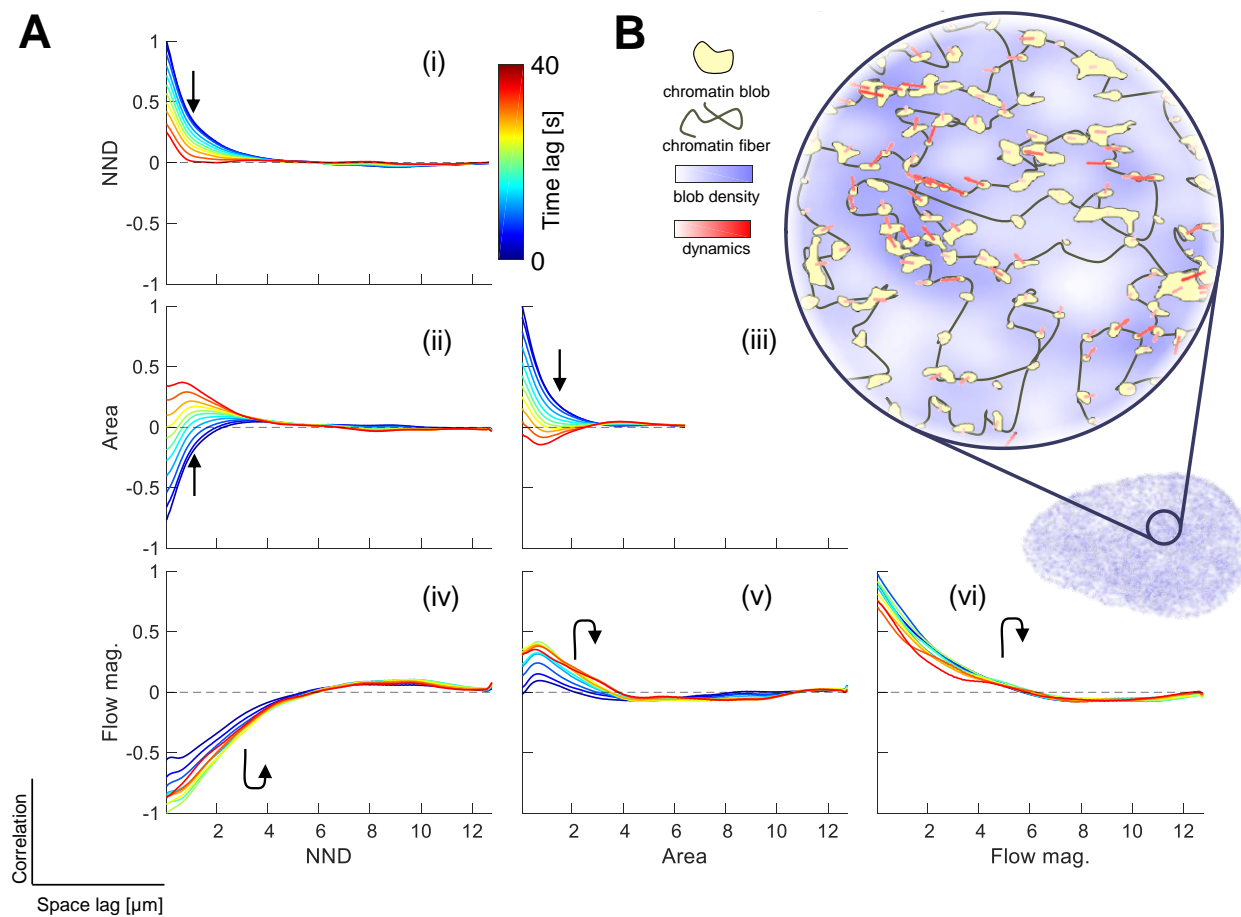
830   **Figure 6**

831

832

SUPPLEMENTARY MATERIAL

Coupling chromatin structure and dynamics by live

super-resolution imaging

R. Barth[1, 2,] K. Bystricky[1] and H. A. Shaban[,1, 3, †, *]

1: Laboratoire de Biologie Moléculaire Eucaryote (LBME), Centre de Biologie Intégrative (CBI), CNRS; University of Toulouse, UPS; 31062 Toulouse; France

2: Department of Bionanoscience, Delft University of Technology, 2628 CJ Delft, The Netherlands

3: Spectroscopy Department, Physics Division, National Research Centre, Dokki, 12622 Cairo, Egypt

†: Present address: Center for Advanced Imaging, Northwest Building, Harvard University, Cambridge, MA, 02138, USA
*: To whom correspondence may be addressed: Haitham A. Shaban. Email hshaban@fas.harvard.edu

847
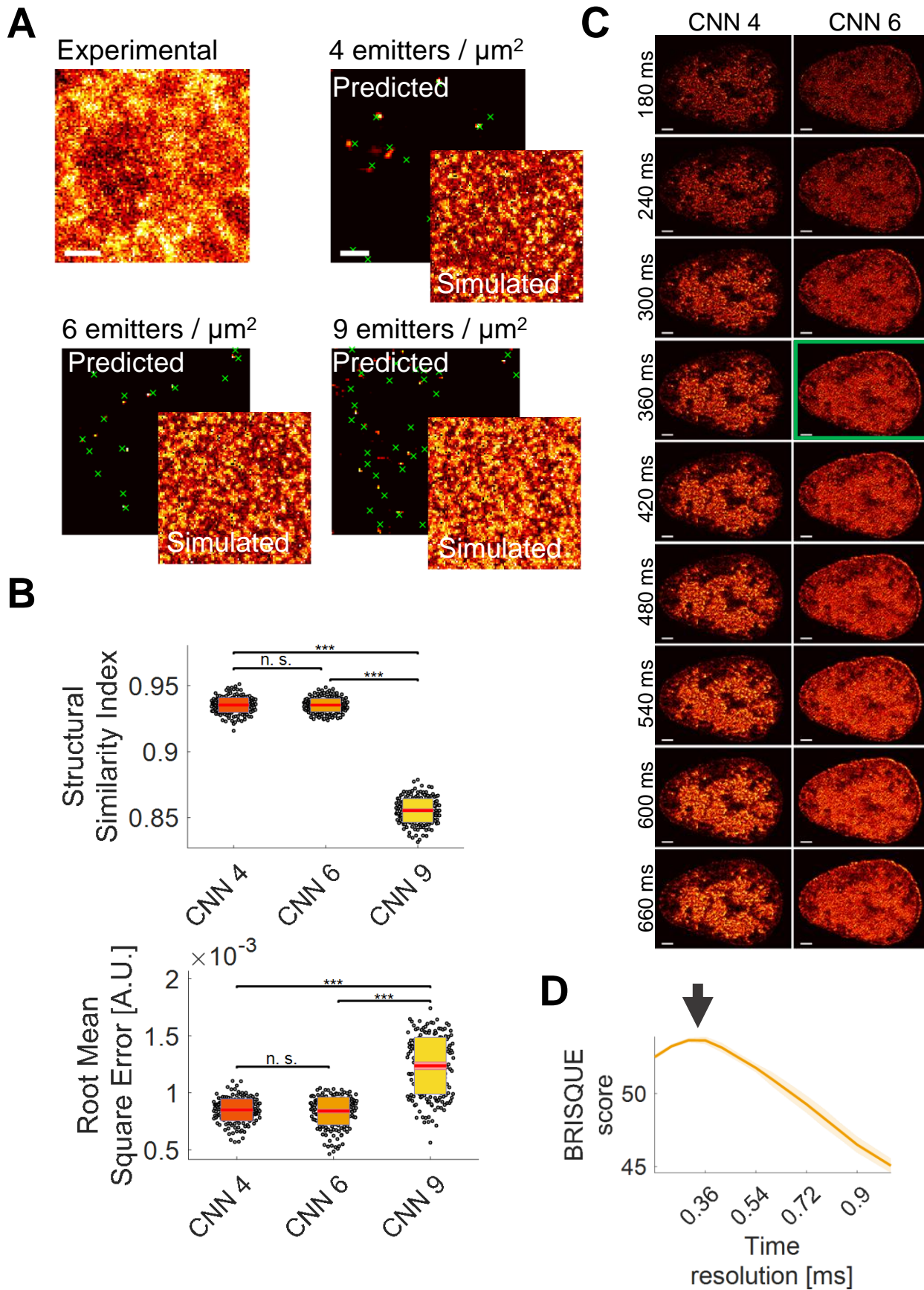
848   **Supplementary Figure 1: CNN training and time-resolution determination. A)** Experimental
849   and simulated widefield images with varying labeling density. Predictions by the trained CNNs are
850   shown as false-color images and the ground truth emitter positions are overlaid as green crosses.
851   Scale bar for experimental widefield image is 2 μm, simulated images are the same size. Scale bar
852   on predictions are 200 nm. **B)** The accuracy of the trained CNNs was evaluated using the Structural
853   Similarity Index and the Root Mean Square Error (Materials and Methods). The CNN trained with
854   9 emitters per μm^2 (CNN 9) performs significantly worse than the other two CNNs. Statistical
855   significance assessed by a two-sample t-test (*** $p < 0.001$). **C)** Predictions from single acquired
856   images are summed over different times from 360 ms to 1020 ms. A subset of reconstructions up
857   to a time resolution of 660 ms are shown for CNN 4 and CNN 6. Scale bar is 2 μm. **D)** The structural
858   image quality as quantified by BRISQUE (*44*) for CNN 6 at varying temporal resolution. The
859   optimal (maximum) value is found at a time resolution of 360 ms.

860
861

862
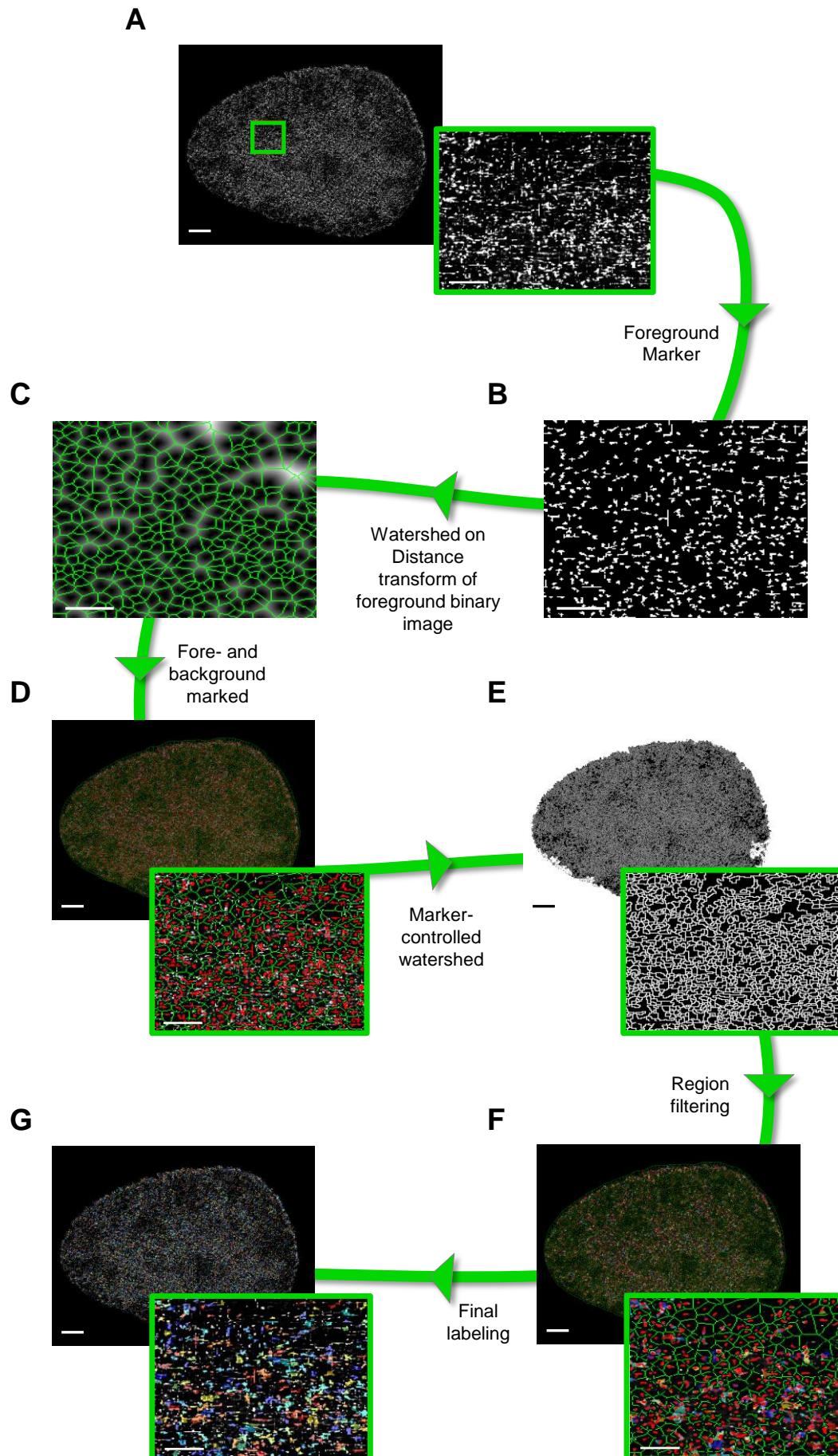
863 **Supplementary Figure 2: Chromatin blob identification pipeline. A)** A grayscale image as
864 output from the Deep-PALM algorithm is to be segmented. Magnified views correspond to the red
865 rectangle. **B)** Foreground pixels are marked by finding the regional maxima. Additionally, very
866 bright pixels (i.e. those with $I > 0.99 \cdot I_{max}$) are marked as foreground. Only the magnification is
867 shown. **C)** The watershed algorithm (without markers) is applied to the distance transform of the
868 foreground mask. The resulting watershed lines represent lines in between pixels marked as
869 foreground and therefore represent pixels of (local) low intensity, i.e. background markers. The
870 background mask is corrected for pixels which nevertheless exert high intensity (i.e. those with $I >$
871 $0.8 \cdot I_{max}$). Only the magnification is shown. **D)** Input image with the foreground (red) and
872 background (green) markers superimposed. **E)** The watershed algorithm is applied to the gradient
873 of the input image with minima imposed on pixels belonging to fore- or background. **F)** The regions
874 defined by watershed lines (the basins) are post-processed in order to keep only those whose mean
875 and median intensity exceed a threshold of $0.1 \cdot I_{max}$. **G)** Resulting segmentation of the input
876 image. Scale bars correspond to 2 µm and 0.5 µm in the full and magnified regions respectively.

877

SUPPLEMENTARY NOTE 1

Segmentation performance

The marker-assisted watershed segmentation pipeline developed to segment chromatin blobs in super-resolved images is tested against other state-of-the-art segmentation algorithms in order to validate its performance. We evaluated our approach against three fully automated improvements of the widely spread watershed algorithm: the enhanced waterfall algorithm, the 'standard' algorithm, and the P-algorithm (*49*). To this end, we simulated images which closely resemble experimental super-resolved images of histone-labeled chromatin. We generated random shapes by thresholding randomly generated 1/f noise and gave intensity to the shapes according to experimental images. An exemplary simulated and experimental image is shown in Supplementary Figure 3A, B. The segmentation result of an exemplary simulated image is shown in Supplementary Figure 3D, I. We used the Rand index as a measure of the similarity of two segmentation algorithms. In particular, the Rand index is computed between the ground truth and the segmentation result of each algorithm as an estimate of the likelihood of a correctly classified element. An image segmentation problem can be formulated as a partitioning of the image pixels into several subsets. Let P denote the set of n pixels to be segmented, $G = \{G_1, \ldots, G_g\}$ denotes the ground truth segmentation of n pixels into g subsets and $R = \{R_1, \ldots, R_r\}$ denotes the resulting segmentation into r subsets from an algorithm to test. The number of agreements between G and R consists of (i) the true positives (TP), i.e. the pairs of elements in P that are in the same subset in G and R and (ii) the true negatives (TN), i.e. the pairs of elements in P that are not in the same subset in G and not in R. Likewise, the number of disagreements consists of (iii) the false negatives (FN), i.e. elements in P that are in the same subset in G but not in R and (iv) the false positives (FP), i.e. elements in P that are not in the same subset in G but that are in R. Taken together, the Rand index expresses the number of agreements over the total number of pairs, i.e. agreements and disagreements (*50*):

$$\text{Rand Index} = \frac{TP + TN}{TP + TN + FN + FP} = \frac{TP + TN}{\binom{n}{2}} \tag{6}$$

The Rand index ranges from 0 to 1 and gives the fraction of matching pairs of pixels in the ground truth and computed segmentation. Our custom marker-controlled watershed algorithm performs significantly better than other tested algorithms, with a Rand index of about 75%.

To further validate the segmentation algorithm, the blob segmentation on experimental images of chromatin (Supplementary Figure 4A) was compared to images, in which emitters were randomly distributed (Supplementary Figure 4B). On random images, the blob density was ~ 19-fold reduced compared to segmentation on experimental images (Supplementary Figure 4C) and the blob area was about one order of magnitude smaller (Supplementary Figure 4D). These results show that blobs were identified due to the appearance of chromatin as blobs and not due to apparent grouping of randomly distributed emitters.

913
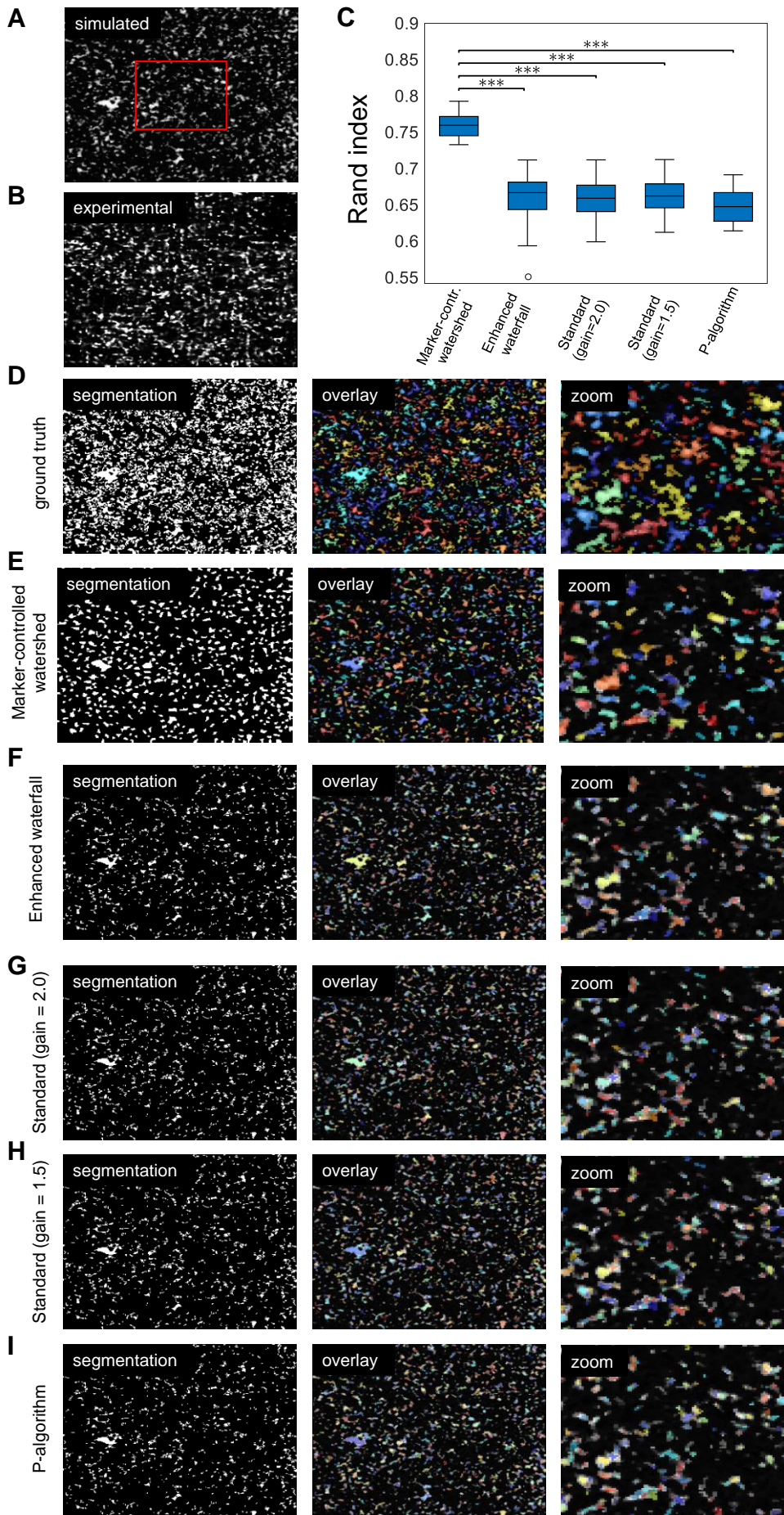
Supplementary Figure 3: Performance of segmentation algorithms on super-resolved images of chromatin *in vivo*. A) Exemplary simulated image for which the ground truth segmentation is known, used to compare different segmentation algorithms. The section in the red triangle is magnified in D-I). **B)** Exemplary experimental image to be compared to the simulated image. **C)** The Rand index reveals that our custom maker-controlled watershed algorithm significantly outperforms all other tested algorithms. Statistical significance assessed from 20 independent segmentation runs by a two-sample t-test (*** p < 0.001). **D)** Binary image (right) displaying the ground truth segmentation of the simulated image. Different segments are randomly colored for clarity and the magnified region marked in A) is shown. **E-I)** Exemplary segmentation results from the tested algorithms.
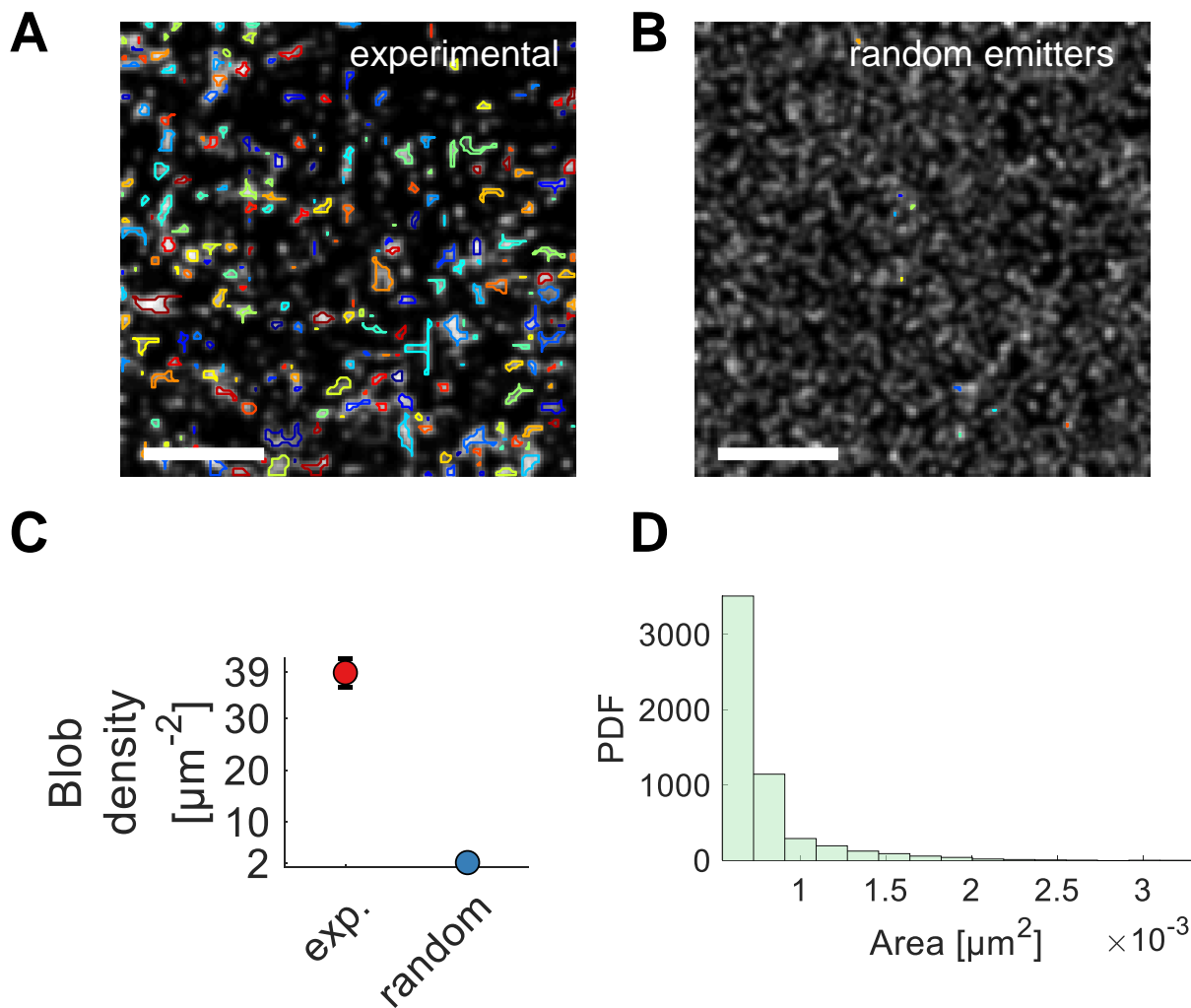
Supplementary Figure 4: Segmentation on images of randomly distributed emitters. A) An exemplary super-resolved image of chromatin *in vivo*, the identified blobs are overlaid and randomly colored. **B)** Emitters were randomly distributed, and the segmentation algorithm was applied to those images. The number of emitter was matched to the number of beads of the modeled chromosomes within the imaging volume (compare Figure 2B). Scale bar is 0.5 μm. **C)** The blob density for blobs identified on experimental images and images containing randomly distributed emitters. Experimental images contained ~20-fold more blobs than could be identified using random images. **D)** Area distribution for blobs identified on images containing randomly distributed emitters (mean ± std.: $(\mathbf{0.4 \pm 0.2}) \cdot \mathbf{10^{-3}}$ μm²).
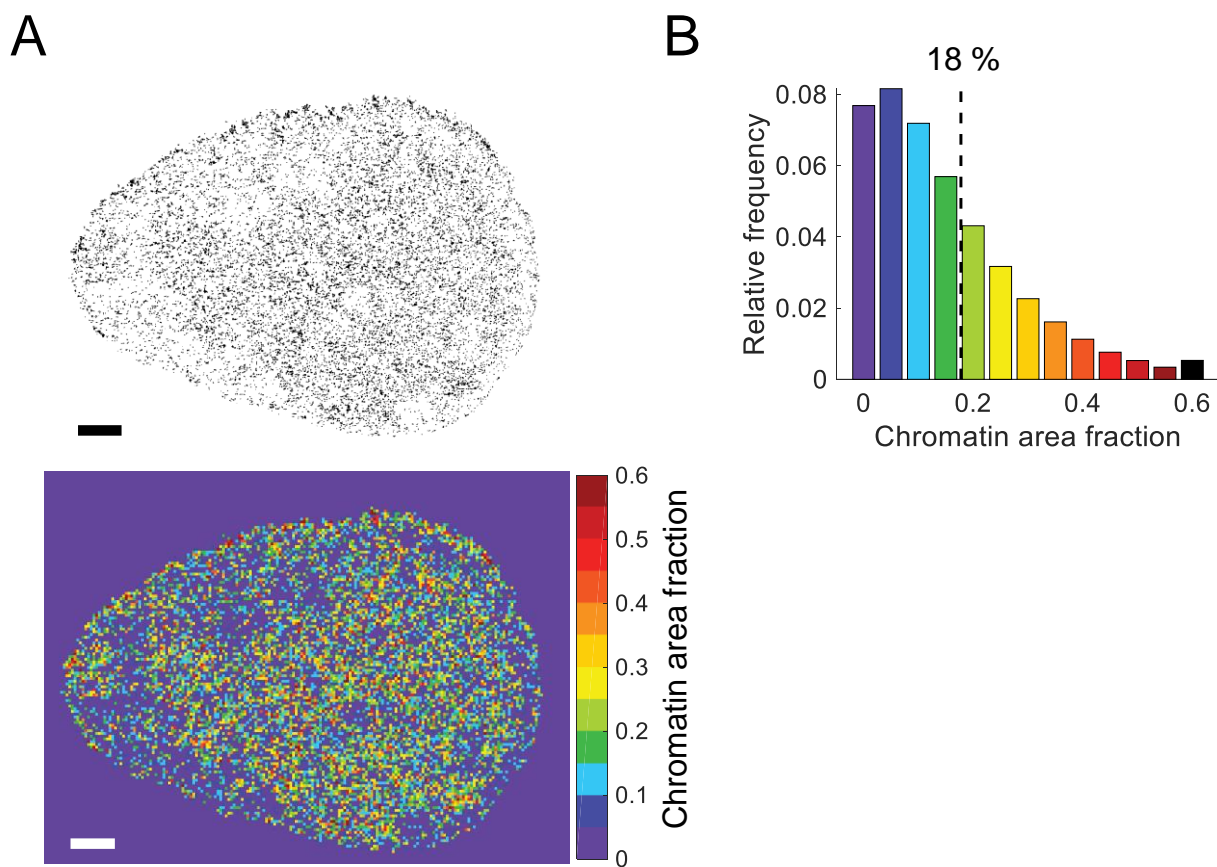
Supplementary Figure 5: Chromatin area fraction. A) Segmented images are divided into boxes with dimensions 120 nm x 120 nm and the chromatin area fraction is computed for each box. Exemplary, a map of chromatin area fractions is shown color-coded from low to high chromatin density (purple to red). Scale bar is 2 µm. **B)** Histogram of the observed chromatin area fractions. The black line denotes 18 ± 14 % (mean $\pm$ std).

SUPPLEMENTARY NOTE 2

Suitability of Optical Flow for super-resolution images of chromatin

Optical Flow is used to compute a flow field between two subsequent images in scenarios in which dynamic information cannot be retrieved from single-particle tracking approaches, for example, due to high labeling densities (*26*). Optical Flow algorithms are generally evaluated with respect to the angular error (AE), a measure for the error in the direction between a computed and a ground truth vector. Likewise, the endpoint error (EE) is a measure for the error in the magnitude. For two computed vectors a and b, the AE and EE are computed as (*25*)

$$AE = \cos^{-1}\left(\frac{ab}{|\mathbf{a}||\mathbf{b}|}\right) \tag{7}$$

and

$$EE = |\mathbf{a} - \mathbf{b}| \tag{8}$$

Current Optical Flow algorithms achieve sub-pixel EE and AE of around 20° for bulk chromatin imaging. Here, we prove that the Optical Flow algorithm used previously for conventional microscopes (*25*, *26*) results in comparable AE and EE values using super-resolved time series of chromatin. To this end, ground truth data is simulated as described previously (*26*). A density of 6 emitters per μm^2 and an acquisition time of 30 ms was used to resemble experimental data (Supplementary Figure 1). The images were either summed up directly in sets of 12 in order to achieve experimental time resolution of 360 ms or first processed by Deep-PALM and then summed. Optical Flow was computed for both sets and the AE and EE were computed. Exemplary simulated images and ground truth vectors, as well as computed flow fields, are superimposed in Supplementary Figure 6A-B. The resulting AE and EE from 20 independent runs are summarized in Supplementary Figure 6C. Optical Flow on super-resolved images did not significantly change the accuracy in direction, however the endpoint error is slightly smaller for flow fields computed on super-resolved images. These results thus validate Optical Flow for the use on super-resolution time series of chromatin.
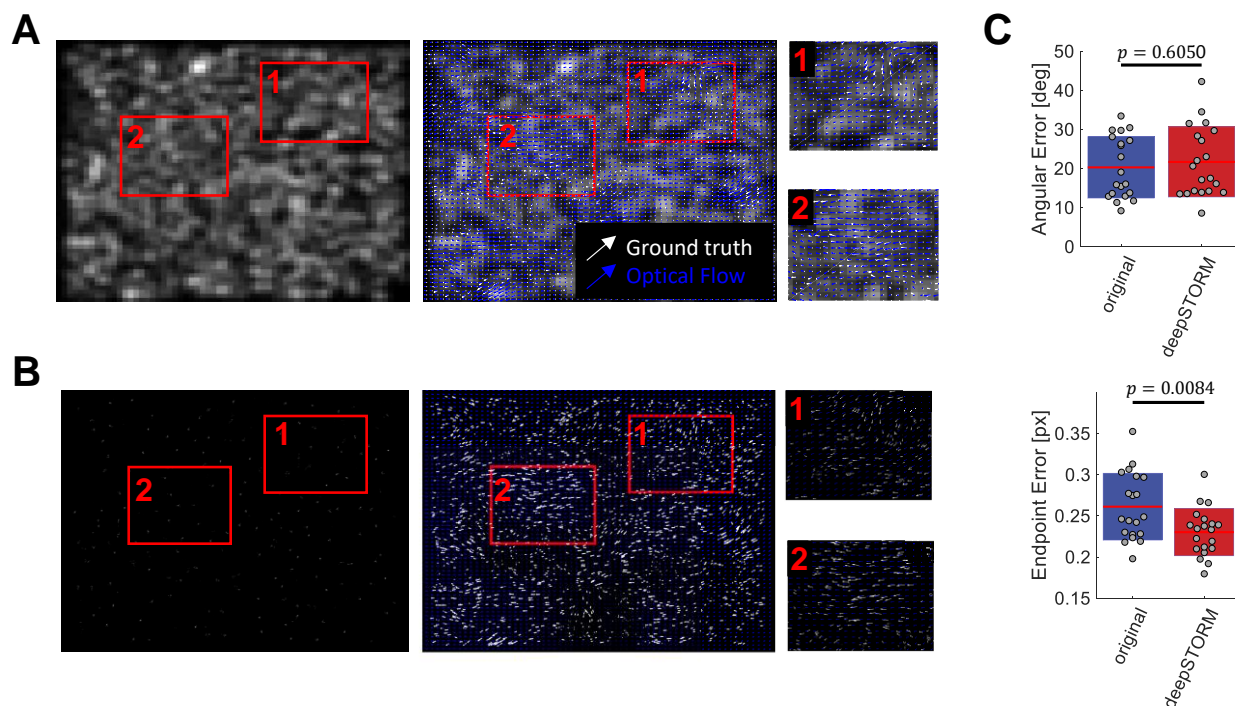
Supplementary Figure 6: Performance of Optical Flow on conventional and super-resolved images. A) Exemplary simulated conventional fluorescence microscopy images (left), ground truth and estimated flow field (middle). Magnified regions as indicated by the red boxes (right). **B)** As

971 A) for images analyzed with Deep-PALM. For visualization, only every eighth vector is shown
972 (Deep-PALM images are up-sampled 8-fold compared to the input images). **C)** Angular and
973 endpoint error over 20 independent sets of simulated images. Statistical significance was
974 determined by a two-sided t-test.

975
976

977 **Supplementary Movie 1: Time series of super-resolved chromatin structure and dynamics.**
978 The centroid positions of each identified blob are mapped onto the nucleus and colored according
979 to their nearest-neighbor distance, area, mean displacement direction, and magnitude. Colors are
980 given such that the respective maximum parameter value over the whole image series is red, the
981 minimum parameter value is blue. Colors thus indicate parameter values relative to the parameter
982 range. Displacement direction is color-coded according to the color-wheel shown.

983
984
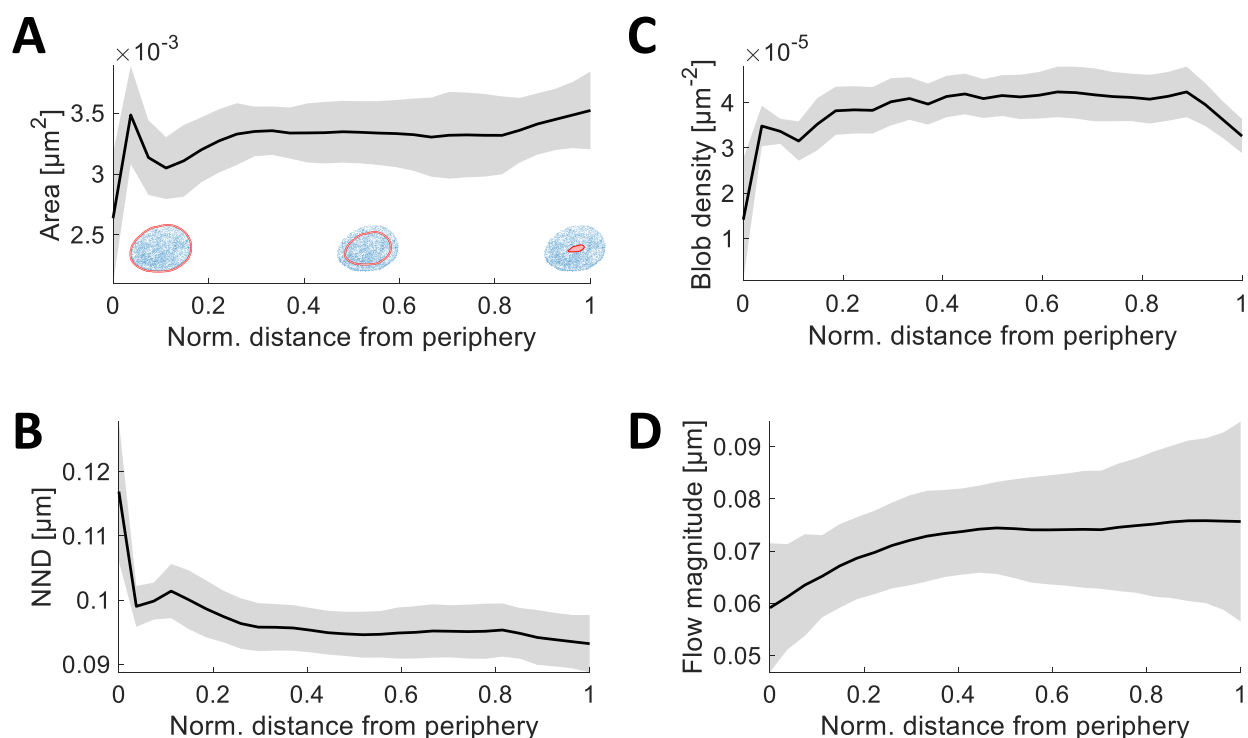
985
986 **Supplementary Figure 7: Structural and dynamic parameters are dependent on the proximity**
987 **to the nuclear periphery. A)** The average area, **B)** NND, **C)** density and **D)** flow magnitude versus
988 the normalized distance from the nuclear periphery (0 is on the periphery and 1 is at the center of
989 the nucleus). Line and shaded area denote the mean $\pm$ standard error.

990
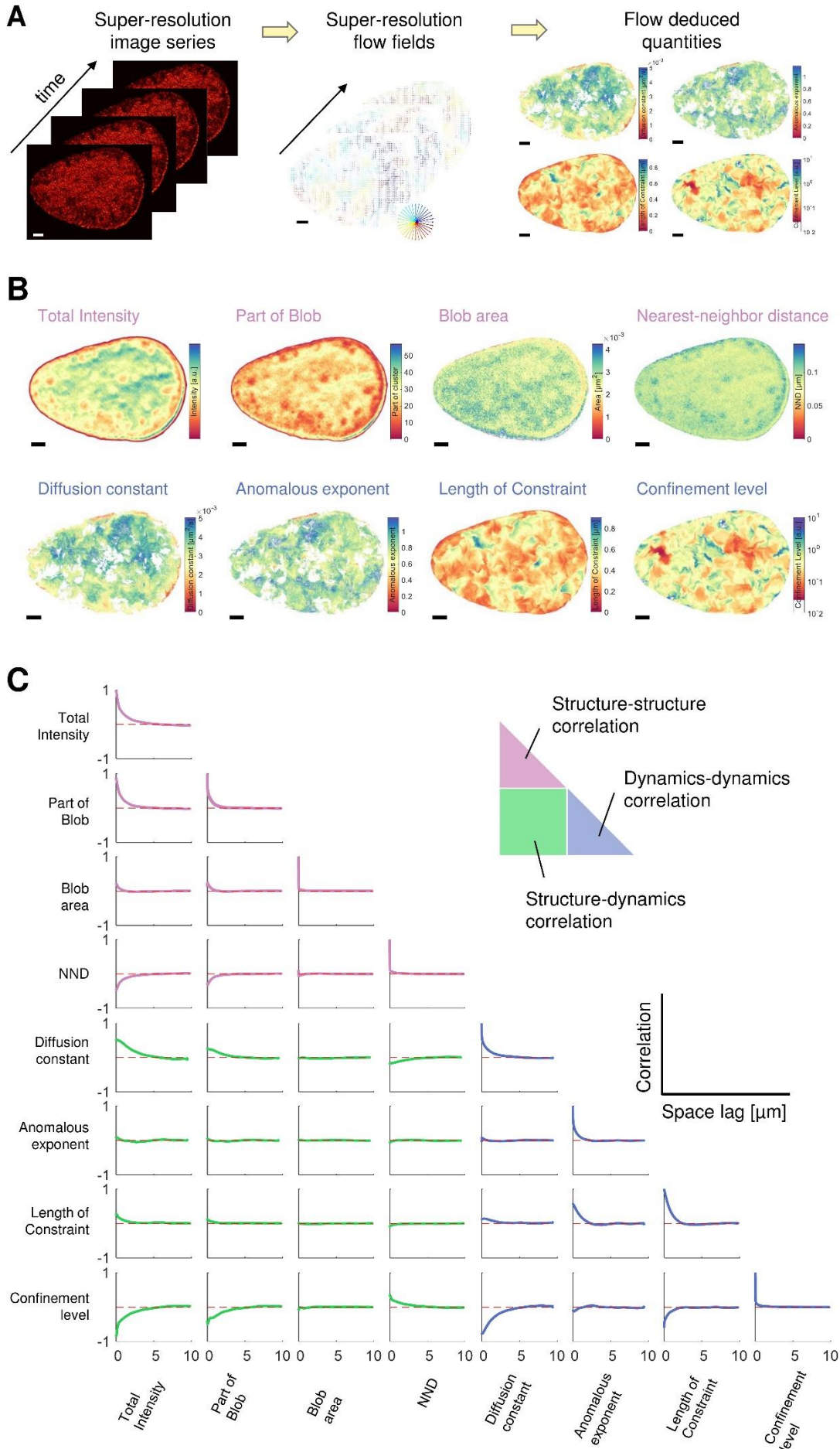
Supplementary Figure 8: Global spatial correlation of structural and dynamic parameters.
A) Illustration of the Hi-D workflow. A time series of super-resolution images (left panel) is input to the Optical Flow algorithm resulting in flow fields with a pixel size of 13.5 nm (middle panel). By trajectory reconstruction and motion classification, quantities describing the underlying bulk motion are computed. **B)** Eight parameters characterizing the global chromatin structure and dynamics during the whole time series are shown. The structural parameters (upper row) are the total intensity of super-resolved images, the counts how often each pixel was identified as part of a chromatin blob, the average blob area per pixel and the average nearest-neighbor distance for each pixel. Dynamic parameters are the diffusion constant and anomalous exponent, which was computed by regression of mean squared displacement curves (Materials and Methods), the length of constraint and the average confinement level. Scale bar is 3 μm. **C)** The spatial correlation between all combinations of structural and dynamic parameters over space lag is shown.

SUPPLEMENTARY NOTE 3

t-SNE and its robustness with respect to distance metrics and perplexity

High-Dimensional parameter space is input to the t-SNE algorithm. The underlying principle is that data points, which are similar with respect to a number of factors (dimensions) lie close in high-dimensional space (employing a certain distance metric). The mapping into lower dimensionality (for instance in 2D) by t-SNE is initialized by assigning each point a random position in 2D (Figure 6A). Illustratively, a set of springs between all data points exert a repelling or attractive force on each other depending on if the current distances between data points in 2D represent the distances between the data points in high-dimensional space. The 2D positions are iteratively refined in order to minimize the divergence between the high-dimensional and two-dimensional distributions.

More specifically, a high-dimensional pairwise distance measure can be defined between all points. The similarity of data points $\mathbf{x_i}$ and $\mathbf{x_j}$ is expressed as the conditional probability, $p_{j|i}$, that $\mathbf{x_i}$ would pick $\mathbf{x_j}$ as its neighbor under the assumption that neighbors are picked in proportion to their probability density under a Gaussian centered at $\mathbf{x_i}$ (*31*):

$$p_{j|i} = \frac{\exp\left(-\|\boldsymbol{x_i} - \boldsymbol{x_j}\|^2/2\sigma_i^2\right)}{\sum_{k\neq i}\exp(-\|\boldsymbol{x_i} - \boldsymbol{x_k}\|^2/2\sigma_i^2)}, \tag{9}$$

and as the symmetrized conditional probabilities

$$p_{ij} = \frac{p_{j|i} + p_{i|j}}{2n}, \tag{10}$$

where n is the number of data points. The variance of the Gaussian, σ_i^2, is determined by a binary search in order to obtain a user-specified value for the *Perplexity*, which is defined as

$$Perplexity(P_i) = 2^{H(P_i)}, \tag{11}$$

where H(P_i) is Shannon's entropy

$$H(P_i) = -\sum_j p_{j|i} \log_2 p_{j|i} \tag{12}$$

and P_i is the conditional probability distribution over all other data points given $\mathbf{x_i}$. The perplexity is, loosely speaking, controlling the number of close neighbors of each point and can have a complex non-linear influence of the resulting distribution of points.

The conditional probability $q_{j|i}$ of two points $\mathbf{y_i}$ and $\mathbf{y_j}$ in the two-dimensional space is modelled by a t-distribution:

$$q_{ij} = \frac{\left(1 + \|\boldsymbol{y_i} - \boldsymbol{y_j}\|^2\right)^{-1}}{\sum_{k\neq l}(1 + \|\boldsymbol{y_k} - \boldsymbol{y_l}\|^2)^{-1}} \tag{13}$$

The algorithm first randomly assigns a position to each data point in two-dimensional space and then iteratively refines the position of data points such as to minimize the Kullback-Leibler (KL) divergence, a natural measure for the mismatch between the joint probability distributions in the high-dimensional space, P, and in the low-dimensional space, Q. Thus, the cost function at every iteration is the KL divergence between P and Q,

$$KL(P||Q) = \sum_i \sum_j p_{ij} \log\left(\frac{p_{ij}}{q_{ij}}\right), \tag{14}$$

which is minimized using a gradient descent method. In other words, the two-dimensional position y_i is modified such as to minimize the KL divergence between P and Q. This minimization scheme depends critically on the conditional probabilities p_{ij} and q_{ij} and therefore on the distance $\|\cdot\|$ between points and the perplexity. We tested the influence of different distance metrics and perplexity values on our data set to exclude artifacts arising through an improper choice of parameters. The following distance metrics were tested:

1042   1) Euclidian distance

$$\|x_i - x_j\| = \sqrt{(x_i - x_j)^T (x_i - x_j)} \tag{15}$$

1043   2) Mahalanobis distance

$$\|x_i - x_j\| = \sqrt{(x_i - x_j)^T S^{-1} (x_i - x_j)} \tag{16}$$

1044   where S is the covariance matrix. The Mahalanobis distance reduces to the Euclidian
1045   distance if S is the identity matrix.
1046   3) Correlation distance

$$\|x_i - x_j\| = 1 - \frac{(x_i - \bar{x}_i)^T (x_j - \bar{x}_j)}{\sqrt{(x_i - \bar{x}_i)^T (x_i - \bar{x}_i)}\sqrt{(x_j - \bar{x}_j)^T (x_j - \bar{x}_j)}} \tag{17}$$

1047   where $\bar{x}$ denotes the average value of x_i.
1048 Perplexity values were varied from 30 to 200. Note that t-SNE is a probabilistic approach since
1049 points are initially distributed randomly in two dimensions. Therefore, multiple runs on the same
1050 data set might result in varying results.
1051 Exemplary t-SNE maps are shown in Supplementary Figure 10A for the tested perplexity values
1052 and distance metrics. Maps are colored corresponding to Figure 6D. The embedding of points in
1053 two dimensions varies greatly among the scenarios. However, the probability of two points being
1054 nearest neighbors is largely conserved and thus ranking of input parameters yield similar results
1055 across the employed scenarios (Supplementary Figure 10B). Rankings are especially robust when
1056 the distance metric is the Euclidian distance or the Mahalanobis distance. When the correlation
1057 distance is employed, the rankings slightly change. Especially, the area of blobs seems to be more
1058 prominent than the flow magnitude, in contrast to rankings when one of the other distance metrics
1059 is used. However, rankings change only to a small extent among the different distance metrics and
1060 perplexity values and the presented results are therefore free of artifacts of t-SNE or algorithm-
1061 dependent parameters.
1062
1063
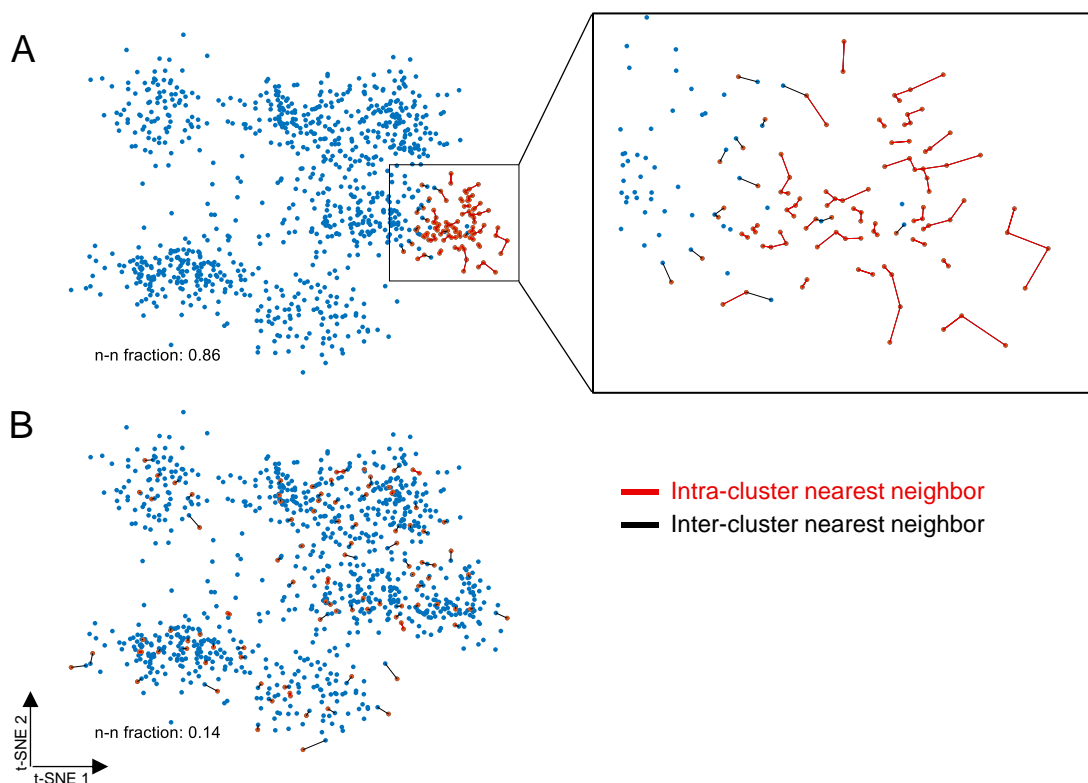
Supplementary Figure 9: Clustering illustration of points within a subset based on nearest-neighbors in t-SNE maps. Dimension reduction using t-SNE results in point clouds in which nearest neighbors in high-dimensional space are conserved and mapped as nearest neighbors in two dimensions. Points at which a number of interest exhibits unusually high/low values are identified (red points). Mapping of two points as nearest neighbors in reduced t-SNE space can be because nearest neighbors belong to the same subset of high/low values of a variable of interest. To quantify this empirical characteristic, the number of nearest neighbors within the same subset in t-SNE space is counted relative to the total number of nearest neighbors of all points within the subset. **A)** A subset mostly contains its own nearest neighbors (86% of nearest neighbors of all points in the subset are contained within the subset). The magnification shows nearest neighbor connections within the subset (red lines) and between points in the subset and points not contained in the subset (black lines). **B)** Points within the subset are distributed over the whole t-SNE space and thus do not form a grouped region. The fraction of nearest neighbor links within the subset is small (14%) compared to the clustered case.
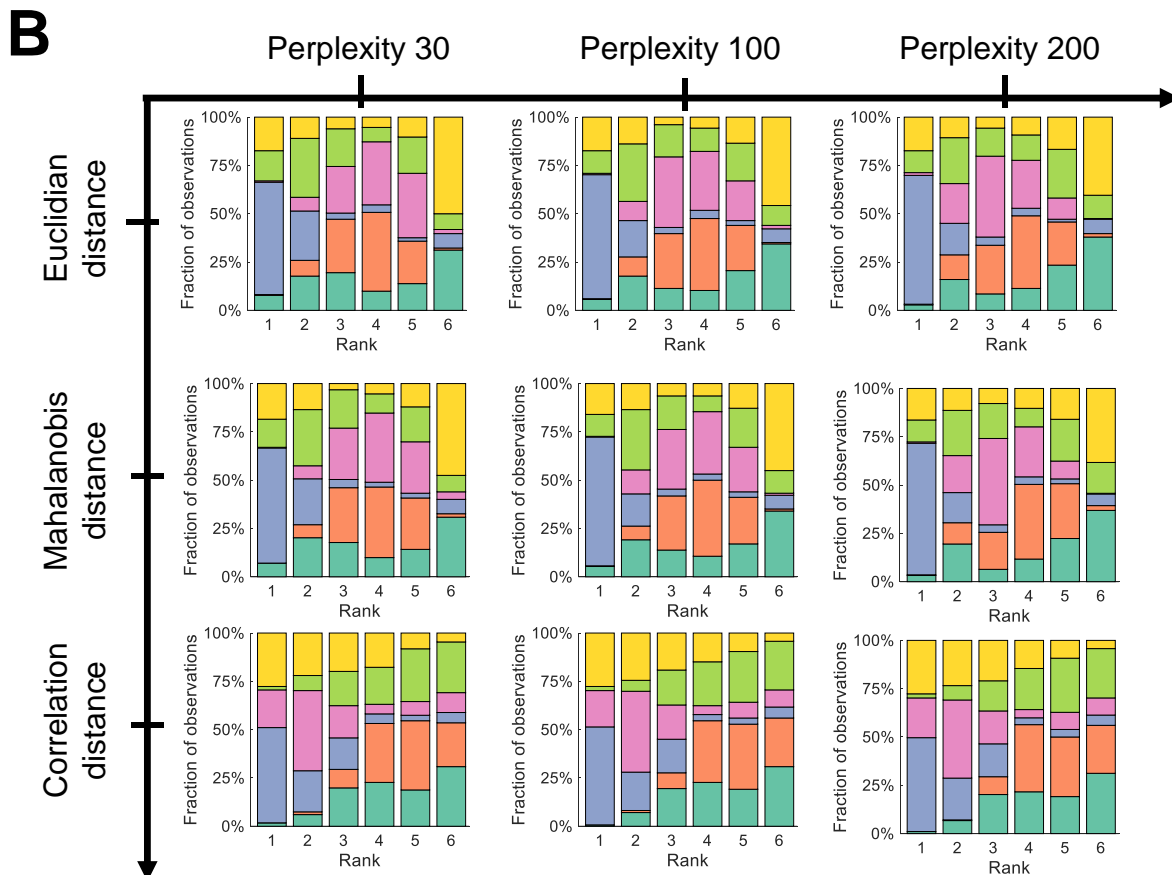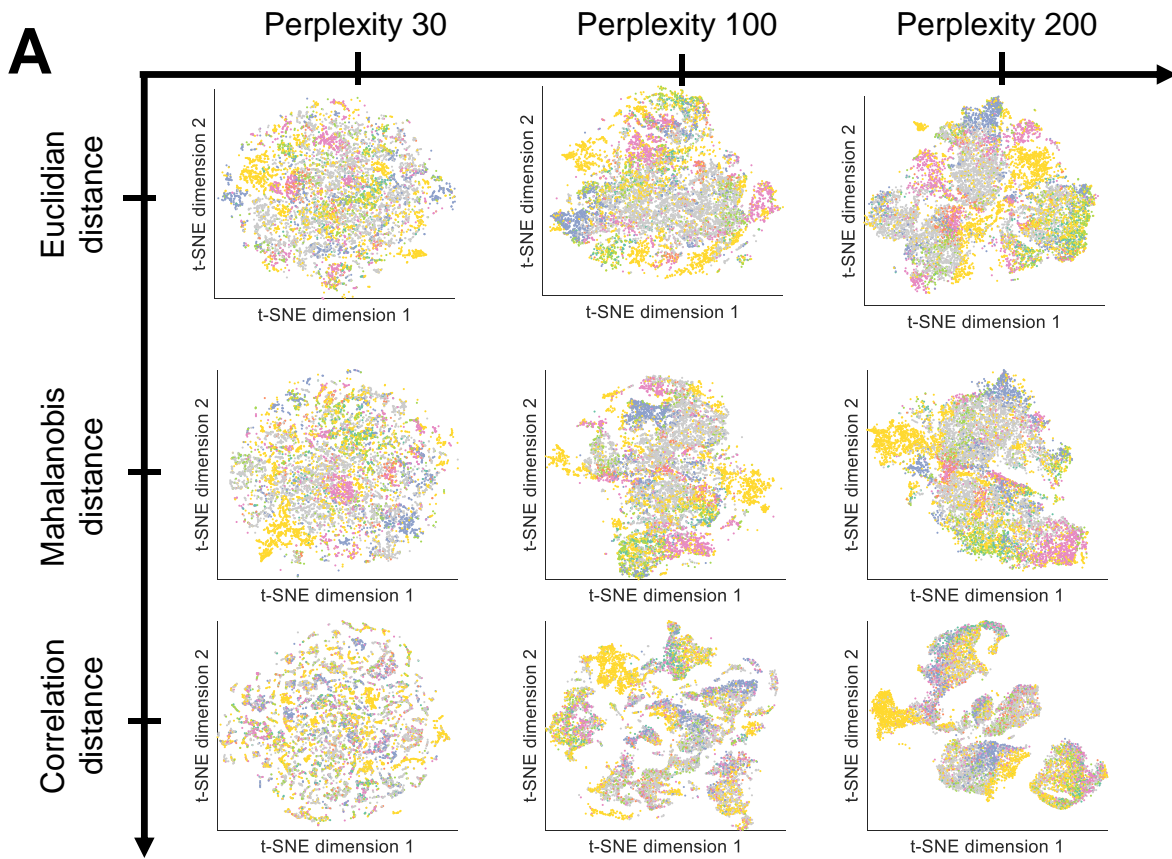
1081 **Supplementary Figure 10: t-SNE for different distance metrics and perplexity values.** We
1082 tested the influence of different distance measures between the high-dimensional data points as well
1083 as variations in the perplexity from 30 to 200 and found that our data are robust to changes in these
1084 parameters within the explored range. **A)** Exemplary t-SNE maps and **B)** feature ranking
1085 considering various distance metrics and values for the perplexity parameter applied to our data.